Ocean Engineering 316 (2025) 119971

Contents lists available at ScienceDirect

Ocean Engineering

journal homepage: www.elsevier.com/locate/oceaneng

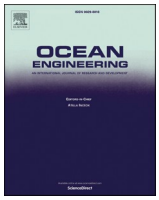

Research paper

Real-time dynamic layout optimization for floating offshore wind farm control

Timothé Jard [a], Reda Snaiki [b,*]

[a] Department of Mechanical Engineering, École de Technologie Supérieure, Université du Québec, Montréal, QC, H3C 1K3, Canada
[b] Department of Construction Engineering, École de Technologie Supérieure, Université Du Québec, Montréal, QC, H3C 1K3, Canada

ARTICLE INFO

Keywords:
Floating offshore wind turbines
Wind farm control
Model predictive control
Dynamic layout optimization

ABSTRACT

Downstream wind turbines operating behind upstream turbines face significant performance challenges due to reduced wind speeds and increased turbulence. This leads to decreased wind energy production and higher dynamic loads on downwind turbines. Consequently, real-time monitoring and control have become crucial for improving wind farm performance. One promising solution involves optimizing wind farm layouts in real-time, taking advantage of the added flexibility offered by floating offshore wind turbines (FOWTs). This study explores a dynamic layout optimization strategy to minimize wake effects in wind farms while meeting power requirements. Three scenarios are considered: power maximization involving two different wind farm configurations and power set-point tracking. The methodology involves a centralized wind farm controller optimizing the layout, followed by wind turbine controllers to meet the prescribed targets. Each FOWT employs model predictive control to adjust aerodynamic thrust force. The control strategy integrates a dynamic wind farm model that considers floating platform motion and wake transport in changing wind conditions. In a case study with a 1x3 wind farm layout of 5 MW FOWTs, the results show a 25% increase in stable energy production compared to a static layout in 1 h for the first scenario. In the second scenario, desired power production was swiftly and consistently achieved. The final scenario demonstrates the control strategy's adaptability to various wind farm layouts.

1. Introduction

Offshore wind turbine technologies have gained remarkable global attention because of their ability to tap into rich wind resources, especially in deep-sea environments (Shah et al., 2021a). In contrast to conventional fixed-bottom offshore structures, which are typically confined to shallower waters due to depth limitations, floating offshore wind turbines (FOWTs) offer the distinct advantage of being deployable in deeper ocean regions (Shah et al., 2021a; Swart et al., 2009). This characteristic allows them to harness the potential of more stable and abundant wind energy sources. However, wind turbines tightly clustered within wind farms experience the wake effect which is characterized by reduced wind speeds and high turbulence levels (Barthelmie et al., 2009). It was estimated that the wake effects have the potential to decrease power generation from each single downstream turbine by as much as 60%, reducing overall wind farm power production by up to 54% (Vermeer et al., 2003; Porté-Agel et al., 2013; Fleming et al., 2014; Nilsson et al., 2015).

Several advanced real-time control methods have emerged in the technical literature, primarily to address the challenge posed by the wake effects and optimize the overall energy production and structural integrity of the wind farm. The control techniques can be broadly classified into two categories: those requiring hardware modifications (Rodrigues et al., 2015; Xu et al., 2021; Li and Wu, 2016; Jahangiri and Sun, 2020, 2022) and those that do not (Kheirabadi and Nagamune, 2019, 2020; Gao et al., 2022; Han and Nagamune, 2020; Escobar Aquino and Nagamune, 2020; Niu et al., 2023). The second control strategy, which eliminates the need for additional hardware, is cost-effective and can be easily implemented in existing utility-scale wind farms. This strategy directly changes the wind turbine parameters, such as the nacelle yaw angle, generator torque, and collective blade pitch angle. Among the various wind farm control methods explored in existing research which do not require additional hardware, two have received extensive attention: power derating (Steinbuch et al., 1988; Johnson and Thomas, 2009; Gonzalez et al., 2013; Annoni et al., 2016; Bitar and Seiler, 2013), often known as axial induction-based control, and

* Corresponding author.
E-mail address: reda.snaiki@etsmtl.ca (R. Snaiki).

https://doi.org/10.1016/j.oceaneng.2024.119971
Received 17 July 2024; Received in revised form 8 November 2024; Accepted 28 November 2024
Available online 6 December 2024

yaw-based wake redirection (i.e., wake steering) (Fleming et al., 2014; Wagenaar et al., 2012; Jiménez et al., 2009; Guntur et al., 2012; Bastankhah and Porté-Agel, 2019; Gebraad et al., 2016; Burton et al., 2011; Lin and Porté-Agel, 2020). The power derating technique reduces the thrust force of an upstream turbine which creates smaller wake, allowing for improved wind flow conditions and boosting power production in downstream turbines. On the other hand, the yaw-based wake redirection is a wind farm control strategy that involves adjusting the orientation or yaw angle of individual wind turbines to redirect the wake generated by upstream turbines away from downstream turbines, thereby optimizing their performance by reducing the overlapping areas between the wakes and downstream rotors. A promising alternative for enhancing the performance of floating wind farms capitalizes on the added degrees of freedom offered by the floating platform to dynamically optimize the wind farm layout (Rodrigues et al., 2015; Kheirabadi and Nagamune, 2019, 2020; Gao et al., 2022; Han and Nagamune, 2020; Escobar Aquino and Nagamune, 2020; Niu et al., 2023; Han et al., 2017; Jard and Snaiki, 2023; Fleming et al., 2015). In this approach, a centralized wind farm controller first identifies the optimal wind farm layout to meet the power requirement (i.e., maximization or regulation) and reduce the wake effects (Gao et al., 2022; Han and Nagamune, 2020; Niu et al., 2023; Boersma et al., 2017). Subsequently, the wind turbine controllers are tasked to achieve the prescribed targets ensuring stable power generation and safe operation (Kheirabadi and Nagamune, 2019, 2020; Han and Nagamune, 2020; Escobar Aquino and Nagamune, 2020; Niu et al., 2023). This can be accomplished through two approaches: one involves actively generating the thrust force to reposition the turbine platform based on actuators such as thrusters and winches (Rodrigues et al., 2015; Xu et al., 2021; Li and Wu, 2016; Sørensen, 2011), necessitating more energy and additional hardware. Alternatively, the second approach involves passive adjustments to the aerodynamic thrust force using existing control inputs, namely the yaw angle, collective blade pitch angle, and generator torque (Kheirabadi and Nagamune, 2019, 2020; Gao et al., 2022; Han and Nagamune, 2020; Escobar Aquino and Nagamune, 2020; Niu et al., 2023; Han et al., 2017; Jard and Snaiki, 2023). Compared to other control techniques, the dynamic layout optimization strategy offers significant advantages since it enables the FOWTs to mitigate the wake effects and maximize energy production without the need to reduce the capacities of upstream turbines, as seen in the axial induction-based control, or employ yaw mechanisms to steer wakes which can negatively impact power generation and introduce stability issues. For example, Fleming et al. (2015) indicated that the wake deflection through the repositioning technique resulted in a 41% improvement in power generation compared to the yaw and tilt misalignment techniques which yielded a 4.6% and 7.6% increase, respectively. Similarly, other studies have reported significant increase in power generation through layout optimization with improvements of up to 53.5% compared to a non-optimized 3x6 layout (Kheirabadi and Nagamune, 2019, 2020).

Despite the recent efforts to enhance the control technique for repositioning the FOWTs by passively manipulating the aerodynamic thrust force (Kheirabadi and Nagamune, 2019, 2020, 2021a; Gao et al., 2022; Niu et al., 2023), limited attention has been given to the more practical scenario involving time-varying free stream wind velocities. This scenario requires sophisticated models capable of swiftly simulating changing wind conditions and customized control techniques to maintain real-time stability. While various control algorithms, such as proportional-integral-derivative (Han and Nagamune, 2020), the H∞ state feedback controller (Escobar Aquino and Nagamune, 2020), and reinforcement learning (Sierra-Garcia et al., 2022; Zhang et al., 2022; Li et al., 2021a, 2021b), have been applied in wind turbine control, designing robust controllers that can effectively handle multiple-input multiple-output systems with numerous constraints and time-varying environmental disturbances remains a challenging endeavor. In addressing these control challenges, model predictive control (MPC) is often favored over alternative control algorithms due to its ability to optimize control inputs over a future time horizon, taking into account system dynamics and constraints, thus enabling more precise and adaptable control in intricate and dynamic processes. Specifically, the MPC algorithm integrates a simplified model of the system, known as the prediction model, into its control law. Using a discrete approach, it calculates the optimal control sequence that minimizes a user-defined objective function over a set time horizon. At each sampling period, the first control action from this sequence is applied to the system, and the prediction model is updated based on the current system states. This process is then repeated at the next sampling period, ensuring continuous optimization and adaptation to changing conditions. While MPC has been applied to various wind turbine control problems (Jard and Snaiki, 2023; Shah et al., 2021b; Raach et al., 2014), none of these studies have yet explored its application in the context of a more realistic wind farm scenario featuring time-varying wind conditions.

This study will focus on exploring a dynamic layout optimization strategy aimed at fulfilling power requirements and mitigating wake effects. Three scenarios will be considered: two of them prioritizing power maximization over different wind farm configurations and one focusing on power set-point tracking. In all scenarios, the objective is to minimize the overlap of wakes with downstream rotors. In the proposed methodology, an initial step involves a centralized wind farm controller identifying the optimal wind farm layout to fulfill power requirements (whether maximizing or regulating power) while also mitigating wake effects. This optimization process is accomplished using Matlab/Simulink. Subsequently, the wind turbine controllers are charged with the task of achieving the designated objectives ensuring both stable power generation and safe operation. Each FOWT is equipped with a model predictive control (MPC) which manipulates directly the aerodynamic thrust force using three control inputs, namely the collective blade pitch angle, the generator torque, and the nacelle yaw angle. The proposed control strategy incorporates an efficient dynamic wind farm model (Kheirabadi and Nagamune, 2021b), which includes the simulation of floating platform motion and wake transport under varying wind conditions and platform movements. In addition, the MPC predictive model is based on a highly efficient dynamic model (Homer and Nagamune,

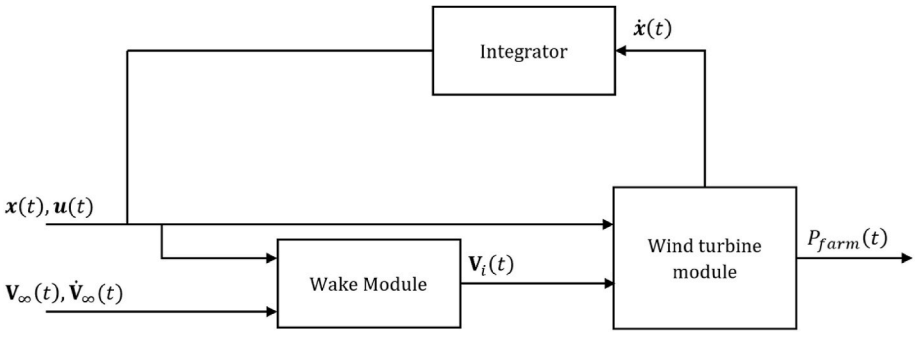

Fig. 1. Block diagram of the FOWFSim-Dyn model.

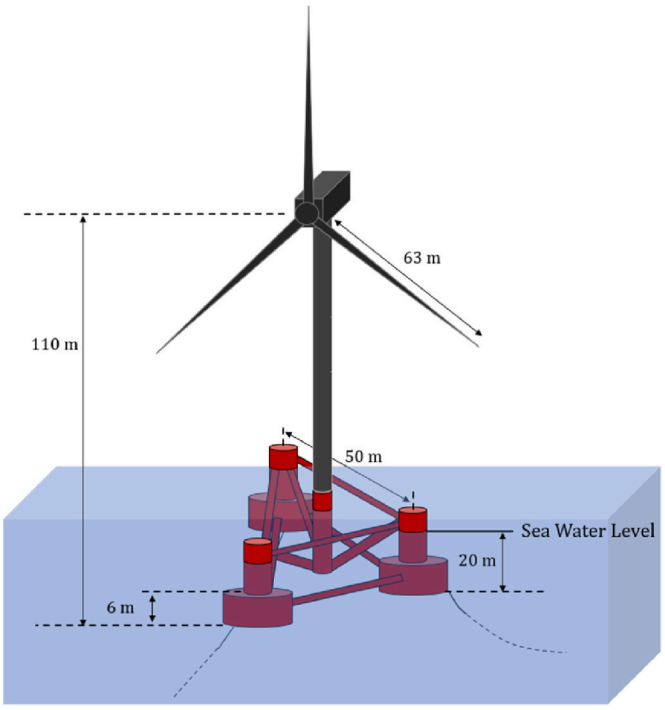

Fig. 2. Schematic representation of the semisubmersible NREL 5-MW FOWT.

2018), designed specifically for real-time control applications. A case study of a wind farm consisting of a 1x3 layout is considered for all scenarios (i.e., power maximization and regulation) using a 5 MW offshore semi-submersible baseline wind turbine developed by the National Renewable Energy Laboratory (NREL) in the United States. To evaluate the controller's performance, it will be compared with a wind farm that lacks a repositioning mechanism.

2. Model description

In this section, an overview of the dynamic parametric wind farm model, FOWFSim-Dyn (Kheirabadi and Nagamune, 2021b), is presented. This model is capable of simulating floating platform motion and the dynamic propagation of wakes under time-varying wind conditions. Specifically, the FOWTs are modeled as a system of particles distributed across a two-dimensional ocean surface. FOWFSim-Dyn comprises two modules: the wake module and the wind turbine module. The wake module solves a one-dimensional momentum conservation equation to simulate the dynamic propagation of wake centerline locations and average velocities, utilizing a constant temporal wake expansion rate to approximate momentum recovery. On the other hand, the wind turbine module simulates the platform dynamics by accounting for aerodynamic, hydrodynamic, and mooring line forces, while computing the power output of the wind farm $P_{farm}(t)$. The block diagram illustrating the interaction between the two modules is presented in Fig. 1. As shown in Fig. 1, the wake module generates the effective wind velocity vector $\mathbf{V}_i(t)$ incident on turbine i's rotor given the states $\boldsymbol{x}(t)$ and inputs $\boldsymbol{u}(t)$ of all turbines, as well as the free stream wind velocity $\mathbf{V}_\infty(t)$ and acceleration vectors $\dot{\mathbf{V}}_\infty(t)$. On the other hand, the wind turbine module calculates the derivative of the state vector, $\dot{\boldsymbol{x}}(t)$, using the effective wind velocity vector $\mathbf{V}_i(t)$ in conjunction with the turbines' states $\boldsymbol{x}(t)$ and inputs $\boldsymbol{u}(t)$.

While the state vector $\boldsymbol{x}(t)$ includes both the position $\mathbf{r}_i(t) := [x_i(t) \quad y_i(t)]^T$ and velocity $\mathbf{v}_i(t) := [v_{x,i}(t) \quad v_{y,i}(t)]^T$ vectors for all floating wind turbines in the wind farm ($i \in \mathscr{T} = \{1, 2, \ldots, N\}$ where N represents the total number of floating wind turbines within the wind farm), the input vector $\boldsymbol{u}(t)$ consists of the effective control inputs $\boldsymbol{u}_i(t) = [\beta_i \quad \tau_{g,i} \quad \gamma_i]^T$ for all wind turbines with $\boldsymbol{u}(t) = [\boldsymbol{u}_1(t) \quad \boldsymbol{u}_2(t) \quad \cdots \quad \boldsymbol{u}_N(t)]$, which are adjusted to meet the control commands. Here, β_i represents the collective blade pitch angle, $\tau_{g,i}$ denotes the generator torque and γ_i is the nacelle yaw angle of turbine i.

Table 1
Main parameters of the semisubmersible NREL 5-MW FOWT.

Parameters	Value
Power rating	5 [MW]
Rotor diameter, Hub height	126 [m], 90 [m]
Gear ratio, Generator efficiency	97, 94.4 [%]
Cut-in, rated, cut-out wind speed	3, 11.4, 25 [m/s]
Cut-in, rated rotor speed	6.9, 12.1 [rpm]
Water depth, Mooring line length	200 [m], 835.5 [m]

In this study, a 5 MW offshore three-bladed wind turbine equipped with a semi-submersible platform, has been considered. The selected platform has been developed by the National Renewable Energy Laboratory (NREL) in the United States and has three cylindrical columns linked to mooring lines, along with a central fourth column responsible for supporting the tower. A schematic representation of the wind turbine is given in Fig. 2, and its main parameters are given in Table 1. Additional information regarding the wind turbine's characteristics is available in references (Jonkman et al., 2009) and (Robertson et al., 2014).

2.1. Wake module

The wake module, alternatively referred to as the aerodynamic module, considers both the free stream velocity and the wind farm layout to simulate the evolution of wakes within the wind farm. This simulation yields the effective wind velocities incident on the turbines. Specifically, in a single wake scenario, the wake module's objective is to determine three time-dependent variables: the position of the wake centerline $y_{w,i}$ relative to the $\hat{x}_i$ axis, the average velocity of the wake at the centerline $\mathbf{v}_{w,i}$ and the wake diameter $D_{w,i}$. These three variables of interest are illustrated in Fig. 3.

With a fixed global frame of reference $(\hat{x}, \hat{y})$ and a local translating frame $(\hat{x}_i, \hat{y}_i)$ linked to each wind turbine, the linear momentum deficit of wake i along $\hat{x}_i$ can be expressed as (Kheirabadi and Nagamune, 2021b):

$$\mathbf{L}_i(\hat{x}_i, t) = \rho_a \frac{\pi}{4} D_{w,i}^2(\hat{x}_i, t)\left[\mathbf{V}_\infty(t) - \left(\mathbf{v}_i(t) + \mathbf{v}_{w,i}(\hat{x}_i, t)\right)\right] \tag{1}$$

where ρ_a is the air density and $\mathbf{V}_\infty := [U_\infty \quad V_\infty]^T$ represents the free stream wind velocity. Setting the time derivative of $\mathbf{L}_i(\hat{x}_i, t)$ to zero, as no external forces impact wake i, yields the following momentum conservation equation:

$$\begin{aligned}\frac{\partial \mathbf{v}_{w,i}(\hat{x}_i, t)}{\partial t} + \left(U_\infty(t) - v_{x,i}(t)\right)\frac{\partial \mathbf{v}_{w,i}(\hat{x}_i, t)}{\partial \hat{x}_i} &= \dot{\mathbf{V}}_\infty(t) - \dot{\mathbf{v}}_i(t) \\ + \frac{2}{D_{w,i}(\hat{x}_i, t)}\frac{dD_{w,i}(\hat{x}_i, t)}{dt}&\left(\mathbf{V}_\infty(t) - \mathbf{v}_i(t) - \mathbf{v}_{w,i}(\hat{x}_i, t)\right)\end{aligned} \tag{2}$$

The wake centerline location can subsequently be determined by solving the following equation:

$$\frac{\partial y_{w_i}(\hat{x}_i, t)}{\partial t} + \left(U_\infty(t) - v_{x,i}(t)\right)\frac{\partial y_{w_i}(\hat{x}_i, t)}{\partial \hat{x}_i} = v_{w_i}(\hat{x}_i, t) \tag{3}$$

Under the assumption of a constant temporal wake diameter expansion rate denoted by k_t, $D_{w_i}(\hat{x}_i, t)$ can be determined by solving the following equation:

$$\frac{\partial D_{w_i}(\hat{x}_i, t)}{\partial t} + \left(U_\infty(t) - v_{x,i}(t)\right)\frac{\partial D_{w_i}(\hat{x}_i, t)}{\partial \hat{x}_i} = k_t \tag{4}$$

The three characteristics variables describing wake i are then

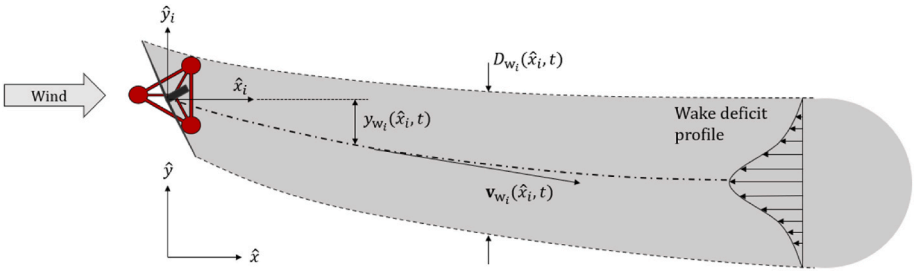

Fig. 3. Schematic representation of the wake zone generated by the turbine *i*.

calculated by subsequently solving Eqs (2)–(4) using the finite difference method and a set of initial conditions (Kheirabadi and Nagamune, 2021b). Following the determination of the average wake centerline velocity, $\mathbf{v}_{w,i}$, from Eq. (2), a Gaussian velocity distribution is adopted to model the variation in velocity with respect to the radial distance from the centerline (as illustrated in Fig. 3). This approach offers a more realistic representation compared to a uniform deficit profile.

To consider the influence of wake interaction in the presence of multiple wind turbines, the effective kinetic energy deficit approach is adopted (Katic et al., 1987). As a result, the effective incident wind velocity vector on the rotor of turbine *i* can be expressed as:

$$\mathbf{V}_i = \left\{ \|\mathbf{V}_\infty\| - \sqrt{\sum_{q\in\mathscr{U}_i} \left(\|\mathbf{V}_\infty\| - \overline{\mathbf{v}}_{w,q\to i} \bullet \mathbf{n}_\infty\right)^2} \right\} \mathbf{n}_\infty \tag{5}$$

where $\mathscr{U}_i = \{1, 2, 3, \ldots, i-1\}$ represents the set of indices of wind turbines located upstream of wind turbine *i*, $\overline{\mathbf{v}}_{w,q\to i}$ represents the effective velocity of wake *q* at wind turbine *i* which is determined using the gaussian assumption for the wake profile (Kheirabadi and Nagamune, 2021b; Bastankhah and Porté-Agel, 2016) and $\mathbf{n}_\infty$ is a unit vector aligned with $\mathbf{V}_\infty$. The predictions of FOWFSim-Dyn for steady-state wake centerlines and normalized velocity profiles were compared with experimental wind tunnel data. This comparison demonstrated satisfactory agreement, indicating the model's suitability for engineering applications (Kheirabadi and Nagamune, 2021b). While the wake model derivation incorporates simplifying assumptions that limit its ultimate fidelity, these simplifications were deemed appropriate for the current study. The primary objective here is to develop a computationally efficient controller suitable for real-time implementation and risk assessment. Employing high-fidelity models based on advanced techniques like Large Eddy Simulation (LES) would be computationally expensive and impractical for real-time applications or risk assessments requiring numerous simulations. FOWFSim-Dyn's accuracy can be further enhanced by incorporating data assimilation techniques in which measurement data are integrated with the model in real-time, potentially leading to more robust simulation results.

2.2. Wind turbine module

Following the determination of the effective wind speed vector at each wind turbine rotor, the wind turbine module leverages a two-dimensional planar model to simulate the platform dynamics. This model employs a Newtonian approach formulated as follows:

$$\dot{\mathbf{v}}_i(t) = \ddot{\mathbf{r}}_i(t) = \frac{\mathbf{F}_{a,i}(t) + \mathbf{F}_{h,i}(t) + \mathbf{F}_{m,i}(t)}{m_i + m_{a,i}} \tag{6}$$

where m_i represents the wind turbine mass, $m_{a,i}$ is the hydrodynamic added mass associated with the *i*th wind turbine, $\mathbf{F}_{a,i}(t)$ is the aerodynamic thrust force, $\mathbf{F}_{h,i}(t)$ is the hydrodynamic force and $\mathbf{F}_{m,i}(t)$ is the mooring line force. Employing the actuator disk theory, the aerodynamic thrust force is directly applied on the turbine's rotor and is expressed for turbine *i* as:

$$\mathbf{F}_{a,i}(t) = \frac{1}{8} C_{t,i} \pi \rho_a D_i^2 \left\|\mathbf{V}_{rel,i}\right\|^2 \mathbf{n}_i \tag{7}$$

where D_i is the rotor diameter, $C_{t,i}$ is the thrust coefficient, $\mathbf{n}_i$ is a unit vector normal to the rotor and $\mathbf{V}_{rel,i}(t)$ is the incident wind speed experienced by turbine *i* expressed as $\mathbf{V}_{rel,i}(t) = \mathbf{V}_i(t) - \mathbf{v}_i(t)$. The thrust coefficient $C_{t,i}$ is a function of blade pitch angle β_i and the tip-speed ratio λ_i, defined as $\lambda_i = \frac{\omega_{r,i} R_i}{V_{\perp,i}}$. In this equation, R_i represents the rotor radius, $\omega_{r,i}$ is the rotor's rotational speed, and $V_{\perp,i}$ is the relative wind speed perpendicular to the rotor surface, expressed as $V_{\perp,i} = \left\|\mathbf{V}_{rel,i}\right\| \cos(\gamma_i - \theta_{rel,i})$, where $\theta_{rel,i}$ is the relative wind angle of $\mathbf{V}_{rel,i}$ with respect to the $\hat{x}$-axis. Using β_i and λ_i, the thrust coefficient $C_{t,i}$ is determined and updated in real time based on the NREL 5-MW C_t-curve (Gao et al., 2022; Han and Nagamune, 2020; Jonkman et al., 2009). The hydrodynamic force is approximated, based on Morison's equation, by summing the forces associated with all submerged elements ($j \in \mathscr{D}_i$) of the floating wind turbine, and is expressed as follows:

$$\mathbf{F}_{h,i}(t) = -\frac{1}{2} \left(\sum_{j\in\mathscr{D}_i} C_{d,i,j} A_{d,i,j} \right) \rho_w \|\mathbf{v}_i\| \mathbf{v}_i \tag{8}$$

where ρ_w is the water density, $C_{d,i,j}$ and $A_{d,i,j}$ are respectively the drag coefficient and the submerged area of the j^{th} component. It should be noted that the effect of platform acceleration is not explicitly included here as an inertial force term. Instead, it is implicitly captured within the overall force model through an added mass. The hydrodynamic added mass associated with turbine *i* is expressed as:

$$m_{a,i} = \rho_w \sum_{j\in\mathscr{D}_i} C_{a,i,j} A_{a,i,j} \tag{9}$$

where $C_{a,i,j}$ and $A_{a,i,j}$ and represent the inertia constant and the added mass reference area of the j^{th} submerged component of turbine *i*, respectively. The restoring force takes into consideration the total number ($\mathscr{M}_i$) of mooring line force vectors acting on the wind turbine *i* and it is expressed as:

$$\mathbf{F}_{m,i}(t) = \sum_{k\in\mathscr{M}_i} -H_{F,i,k} \frac{\mathbf{r}_{F/A,i,k}}{\left\|\mathbf{r}_{F/A,i,k}\right\|} \tag{10}$$

where $H_{F,i,k}$ is the magnitude of the horizontal tension component corresponding to the k^{th} mooring line of the i^{th} turbine, determined by solving the static differential equations governing a suspended cable, which can be either partially resting on or entirely elevated above the seabed (Kheirabadi and Nagamune, 2021b), and $\mathbf{r}_{F/A,i,k}$ is the horizontal position vector from the anchor to the corresponding fairlead of the k^{th} mooring line. It should be noted that the FOWFSim-Dyn wind turbine module employs a two-degree-of-freedom representation for each turbine. This simplification neglects the heave, yaw, pitch, and roll motions of the floating platform. While this omission limits the model's ability to

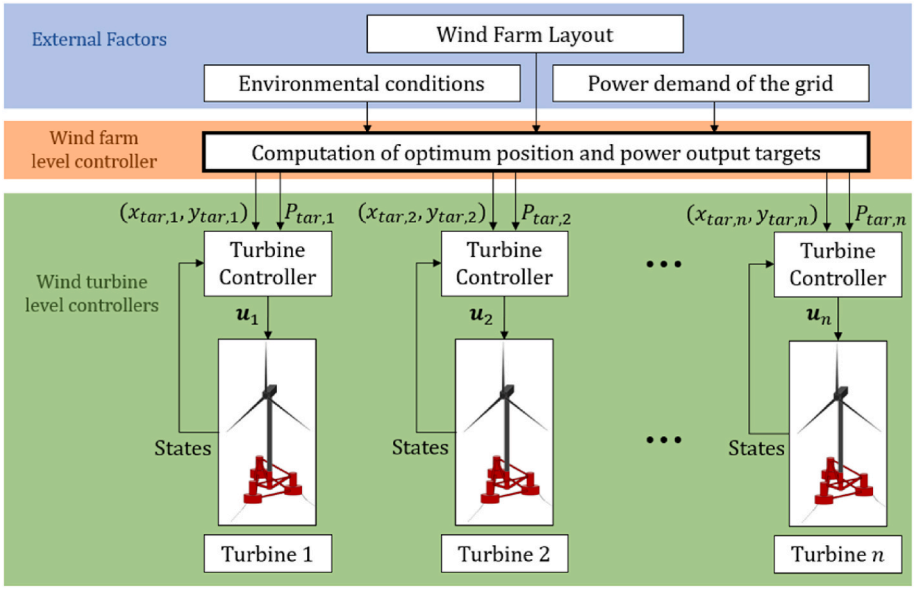

Fig. 4. Block diagram of the control system.

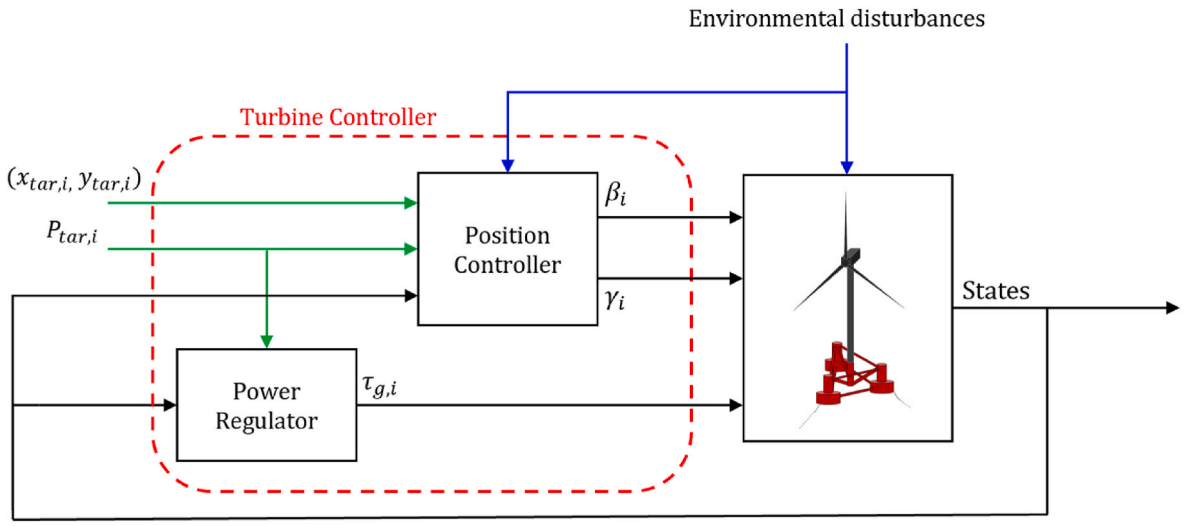

Fig. 5. Block diagram of the wind turbine controller.

fully capture the complex effects of ocean waves and fluctuating wind conditions on platform rotation, it remains computationally efficient and well-suited for wind farm controller design and testing purposes. Additionally, the platform dynamics module within FOWFSim-Dyn has been successfully validated against results obtained from FAST (Kheirabadi and Nagamune, 2021b).

Using the output from both the wake and wind turbine modules, the total wind farm power can be computed as follows:

$$P_{farm}(t) = \sum_{i \in \mathcal{F}} P_{out,i}(t) \tag{11}$$

where $P_{out,i}$ is the instantaneous power output of turbine i expressed as:

$$P_{out,i}(t) = \tau_{g,i}\omega_{g,i}\eta_{g,i} \tag{12}$$

where $\omega_{g,i}$ is the generator speed of turbine i and $\eta_{g,i}$ is the generator conversion efficiency of turbine i.

3. Control design

3.1. Control structure

To achieve the targeted power output and mitigate the wake effects, the proposed controller system consists of two main levels: the wind farm controller (orange zone in Fig. 4) and the individual wind turbine controllers (green zone in Fig. 4, illustrated in more detail in Fig. 5). It should be noted that the subscript "*tar*" indicates the target power and position which are communicated from the wind farm controller to the wind turbine controllers. Further insights into each controller are elaborated upon in the subsequent sections.

3.2. Wind farm controller

The wind farm controller calculates the optimal setpoints (i.e., optimal wind turbine coordinates and individual power target), considering environmental conditions (such as wind), wind farm layout and the power demand from the electrical grid (blue zone in Fig. 4).

Achieving these optimal setpoints requires solving an optimization problem. For instance, in the context of power maximization, the optimization problem can be formulated as follows:

$$\underbrace{\max}_{setpoints}\left(P_{farm}\right);\ \text{subject to}\begin{cases}\text{safety limits}\\ \text{system contraints}\\ \text{wake limitation}\\ \dots\end{cases} \tag{13}$$

To ensure the reliable and safe operation of floating wind turbines under diverse environmental conditions, several constraints must be satisfied for each turbine, including the following:

$$\begin{cases} x_{min,i} \le x_{tar,i} \le x_{max,i} \\ y_{min,i} \le y_{tar,i} \le y_{max,i} \\ \left|\left(\gamma_i\left(x_{tar,i}, y_{tar,i}\right) - \theta_{rel,i}\left(x_{tar,i}, y_{tar,i}\right)\right|\right. \le (\gamma - \theta_{rel})_{max} \\ V_{min} \le V_i\left(x_{tar,i}, y_{tar,i}\right) \end{cases} \tag{14}$$

where $(x_{min,i}, x_{max,i})$ & $\left(y_{min,i}, y_{max,i}\right)$ represent the minimum and maximum permissible displacements of floating platform i in the $(\hat{x}, \hat{y})$ plan to maintain a safe positioning (e.g., to avoid obstacles or prevent collision between turbines). Additionally, $(\gamma - \theta_{rel})_{max}$ represents the maximum permissible misalignment between the turbine rotor and the incident wind, minimizing any extra aerodynamic loads on the blades. Furthermore, to enhance wind turbine performance and prolong its operational lifespan, it is crucial to guide the controller to minimize, whenever feasible, the areas affected by wakes, which are known to be a source of various fatigue-related issues. This consideration is addressed in the final constraint, ensuring that the incident wind on each turbine in the optimal layout remains above a minimum threshold V_{min} (adjusted based on the free-stream wind speed). In this study, the optimization problems are resolved using the Simulink Design Optimization toolbox (The MathWorks and Inc, 2023), employing the pattern search algorithm (Powell et al., 1994). Specifically, this iterative heuristic method relies on successive simulations (i.e., episodes) to explore the search space. The objective function is then evaluated at the end of each episode to obtain the optimal solutions, which will subsequently be employed as setpoints in the various control scenarios. In this study, the duration of each of these episodes are fixed at 2000 s to allow for a complete repositioning. To simplify the optimization process and reduce computational overhead, a constant axial induction factor ($a = 0.3$) was adopted. This substitution is made to avoid dealing with several control inputs during the acquisition of optimal solutions and, consequently, to facilitate the resolution of the optimization problems. It's important to note that this simplification is only applied during the optimization calculations performed by the wind farm controller (orange zone in Fig. 4). Once the optimal positions are determined, they are sent to the individual wind turbine controllers, which can then use conventional control inputs to achieve the desired positions.

3.3. Wind turbine controller

The wind turbine controller associated with the i^{th} turbine is designed to reposition the floating platform, aligning it with its designated coordinates $\left(x_{tar,i}, y_{tar,i}\right)$, and to maintain the generated power around the specified target value $(P_{tar,i})$, as directed by the wind farm controller (orange zone in Fig. 4). In this study, the control strategy requires no external actuators or additional hardware, as it directly manipulates the aerodynamic thrust force. This feature makes it suitable for both new and existing offshore wind turbines. Specifically, each wind turbine i has three control inputs, namely the collective blade pitch angle β_i, the generator torque $\tau_{g,i}$, and the nacelle yaw angle γ_i. The nacelle yaw angle steers the thrust force direction, as it is assumed to be perpendicular to the rotor plane. When misaligned with the wind direction, the force decomposes into two components: one along the wind and another perpendicular to it, inducing lateral platform motion. Blade pitch angle adjustments influence the thrust force magnitude since the thrust coefficient depends on both blade pitch angle and tip-speed ratio (itself a function of pitch angle). Similarly, the generator torque affects the thrust magnitude by altering the generator speed, which in turn influences the tip-speed ratio and subsequently the thrust coefficient. Moreover, it regulates the generator speed and power extraction. It should be noted that, at very low wind speeds, this strategy may not be effective. The approach relies on a balance between the aerodynamic thrust force and the mooring lines forces. At low wind speeds, the generated thrust may be insufficient to overcome the forces from the mooring lines. Furthermore, to generate sufficient thrust force, the strategy utilizes pitch-to-stall regulation, which can cause the blades to enter complete aerodynamic stall and potentially shut down the turbine at low wind speeds. However, while this strategy is limited to wind speeds above the rated value, this is not a significant concern, as the wake effect at low wind speeds is typically too weak to justify turbine repositioning.

The wind turbine controller comprises two primary subsystems: the power regulator, responsible for maintaining the specified power level $P_{tar,i}$ consistently, and the position controller, which governs the platform's movement, as depicted in Fig. 5. Further details regarding each control subsystem will be presented in the following sections.

3.3.1. Power regulator

The control law governing the power regulator is based on the constant power strategy (Jonkman et al., 2009). Specifically, for the wind turbine i, the regulator provides the torque $\tau_{g,i}$ necessary to generate the desired power level $P_{tar,i}$ as determined by the following equation:

$$\tau_{g,i} = \frac{P_{tar,i}}{\eta_{g,i}\omega_{g,i}} \tag{15}$$

where $\omega_{g,i}$ is the generator speed and $\eta_{g,i}$ is the generator's conversion efficiency.

3.3.2. Position controller

The goal of the position controller is to relocate the floating platform of turbine i to the target position $\left(x_{tar,i}, y_{tar,i}\right)$, as provided by the wind farm controller. To achieve this objective, the controller receives the current system states, such as position, along with perturbations and generates appropriate control inputs β_i and γ_i to modify the aerodynamic thrust force. In this study, a model predictive control (MPC) is employed to achieve these control objectives. The MPC model relies on a dynamic representation of the system's process. This internal representation is used to aid in predicting the necessary control actions while considering the system's constraints.

In this study, an efficient control-oriented dynamic model (Homer and Nagamune, 2018) suitable for real-time control applications has been employed as the prediction model for the MPC controller. This selection was made to minimize the computational costs and facilitate controller design. The model represents the overall dynamics of the floating wind turbine while reducing the number of degrees of freedom (DOFs) to six platform DOFs and two drivetrain DOFs, resulting in a total of 15 states. The derivation of this model is based on a Newtonian approach, treating the FOWT as a rigid body subjected to various forces. The model is expressed in a state-space format as follows:

$$\dot{\boldsymbol{X}} = f(\boldsymbol{X}, \boldsymbol{u}, \boldsymbol{v}, \boldsymbol{w}) \tag{16}$$

where $\boldsymbol{u}$ is the control inputs vector, $\boldsymbol{v}$ and $\boldsymbol{w}$ are the vectors referring to the environmental disturbances, with $\boldsymbol{v}$ corresponding to the wind and $\boldsymbol{w}$ to the waves. Finally, the vector $\boldsymbol{X}$ refers to the system states, which include translational coordinates of the floating platform (surge x, sway y and heave z), rotational coordinates (roll θ_x, pitch θ_y and yaw θ_z), their derivatives, rotor rotational speed ω_r, generator rotational speed ω_g and

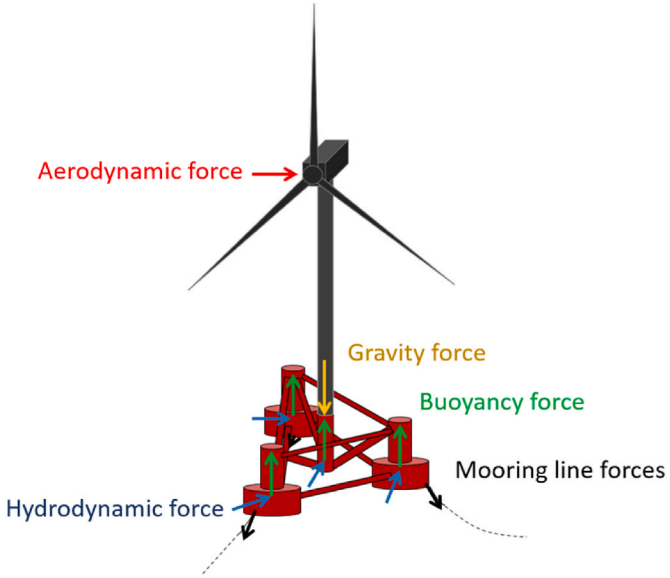

Fig. 6. Schematic representation of the forces acting on a FOWT.

the shaft deflection angle $\Delta\theta_r$. The system dynamics are then captured by the nonlinear function, f, which relates the system inputs, disturbances, and states as expressed by the following equation:

$$f(\boldsymbol{X},\boldsymbol{u},\boldsymbol{v},\boldsymbol{w}) = \left[\dot{x},\dot{y},\dot{z},\dot{\theta}_x,\dot{\theta}_y,\dot{\theta}_z,\vec{f}_F,\vec{f}_T,f_Q,\Delta\dot{\theta}_r\right]^T \tag{17}$$

where $\vec{f}_F$, $\vec{f}_T$ and f_Q are respectively the sum of forces, torques and shaft torque acting on the system. These terms are expressed by the following equations:

$$\vec{f}_F(\boldsymbol{X},\boldsymbol{u},\boldsymbol{v},\boldsymbol{w}) = (mI_3 + \mathrm{diag}[\boldsymbol{m}_a])^{-1}\,(\mathbf{F}_A + \mathbf{F}_B + \mathbf{F}_C + \mathbf{F}_D) \tag{18}$$

$$\vec{f}_T(\boldsymbol{X},\boldsymbol{u},\boldsymbol{v},\boldsymbol{w}) = \left(\underline{R}_{rot}\underline{I}_g^{-1}\underline{R}_{rot}^T\right)\,(\mathbf{T}_A + \mathbf{T}_B + \mathbf{T}_C + \mathbf{T}_D) \tag{19}$$

$$f_Q(\boldsymbol{X},\boldsymbol{u},\boldsymbol{v}) = \begin{bmatrix} \frac{1}{J_r}\left(\frac{P_{aero}}{\omega_r} - k_r(\Delta\theta_r) - b_r(\Delta\dot{\theta}_r)\right) \\ \frac{1}{J_g}\left(-\tau_g + \frac{k_r}{N_{GR}}(\Delta\theta_r) + \frac{b_r}{N_{GR}}(\Delta\dot{\theta}_r)\right) \end{bmatrix} \tag{20}$$

where $\mathbf{F}_A$ is the aerodynamic force, $\mathbf{F}_B$ is the buoyancy force including the force of gravity, $\mathbf{F}_C$ is the mooring line force, $\mathbf{F}_D$ is the hydrodynamic drag/inertia force while $\mathbf{T}_A$, $\mathbf{T}_B$, $\mathbf{T}_C$ and $\mathbf{T}_D$ are their respective torques acting on the center of gravity of the structure, J_r and J_g are the rotor and generator inertias, respectively, k_r and b_r are the stiffness and damping of the drivetrain, P_{aero} is the aerodynamic power, N_{GR} is the gear ratio, $\underline{R}_{rot}$ is a rotation matrix and $\underline{I}_g$ is an inertia tensor. A schematic representation of the forces acting on a FOWT is depicted in Fig. 6. The aerodynamic force, $\mathbf{F}_A$, is estimated using the actuator disk theory and applied at a single point coinciding with the center of the rotor, aligned with the shaft's direction. The force $\mathbf{F}_B$ is the sum of the gravitational force, which acts at the center of gravity of the FOWT platform, and the resultant force from the application of Archimedes' principle on each platform cylinder. The mooring line force $\mathbf{F}_C$ is determined using a quasi-static, two-dimensional single-cable model (Jonkman, 2009). The hydrodynamic force, $\mathbf{F}_D$, acting on the platform is determined by segmenting the platform and applying Morison's equation to each segment. The updated system states can be determined through straightforward integration of $\dot{\boldsymbol{X}}$, derived from Eq. 16. The accuracy of the proposed wind turbine model was verified through comprehensive validation against the established FAST simulation software (Homer and Nagamune, 2018). This involved comparing the time responses of the nonlinear model (with all degrees of freedom enabled) to those obtained from FAST under realistic wind, wave disturbances, and all control inputs. The results demonstrated very good agreement with minor discrepancies. This successful validation underscores the model's suitability for various control applications, as evidenced by its successful implementation in prior studies (Han and Nagamune, 2020; Escobar Aquino and Nagamune, 2020; Shah et al., 2021b). Further details regarding the model and its parameters can be retrieved from (Homer and Nagamune, 2018).

Table 2
Imposed constraints, saturations, and rate limits on each controller in the control process.

Control Inputs	Saturation	Rate Limit
β_i	[−30, 0] [deg]	[−8, 8] [deg/s]
$\tau_{g,i}$	[0, 47.402] [kN•m]	[−15, 15] [kN•m/s]
γ_i	[−60, 60] [deg]	[−0.3, 0.3] [deg/s]

The nonlinear model represented by Eq. (16) is linearized around carefully chosen equilibrium points, denoted as $\boldsymbol{p}_{eq} = [\boldsymbol{X}_0,\boldsymbol{u}_0,\boldsymbol{v}_0,\boldsymbol{w}_0]^T$ by solving the following equation:

$$f(\boldsymbol{X}_0,\boldsymbol{u}_0,\boldsymbol{v}_0,\boldsymbol{w}_0) = \mathbf{0} \tag{21}$$

This results in the subsequent linearized model, represented as:

$$\delta\dot{\boldsymbol{X}} = A\delta\boldsymbol{X} + B\delta\boldsymbol{u}_{MPC} + C\delta\boldsymbol{v} \tag{22}$$

where $\boldsymbol{u}_{MPC} = [\beta \quad \gamma]^T$ represents the MPC control inputs while A, B and C are the equivalent linearized matrices which are determined based on the Jacobians of the function f at the equilibrium point $\boldsymbol{p}_{eq}$ as:

$$A = \left.\frac{\partial f}{\partial \boldsymbol{X}}\right|_{\boldsymbol{p}_{eq}} \quad B = \left.\frac{\partial f}{\partial \boldsymbol{u}_{MPC}}\right|_{\boldsymbol{p}_{eq}} \quad C = \left.\frac{\partial f}{\partial \boldsymbol{v}}\right|_{\boldsymbol{p}_{eq}} \tag{23}$$

Based on the linearized model, the MPC controller employs an iterative approach to determine the optimal control actions. Specifically, the controller utilizes a discrete-time approach, seeking the optimal sequence of control inputs over the control horizon N_m that minimizes a cost function J over the prediction horizon N_p while accounting for the system constraints. This process is then repeated at each time step. The cost function J can be expressed as:

$$J = \sum_{k=i+1}^{i+N_p} \left\|Q\left[\boldsymbol{Y}_k - \boldsymbol{Y}_{ref}\right]\right\|^2 + \sum_{k=i}^{i+N_m-1} \left\|R\left[\boldsymbol{u}_{MPC,k} - \boldsymbol{u}_{MPC,k-1}\right]\right\|^2 + \sum_{k=i}^{i+N_p-1} \left\|S\left[\boldsymbol{u}_{MPC,k} - \boldsymbol{u}_{MPCref,k}\right]\right\|^2 \tag{24}$$

where Q, R and S are weight matrices which are designed to penalize excessive outputs errors and regulate the excessive use of the control inputs (i.e., blade pitch and nacelle yaw), $\boldsymbol{Y}$ is the output vector, representing the desired states being controlled (e.g., surge, sway and generator rotational speed), which is optimized to match the target vector $\boldsymbol{Y}_{ref}$ and $\boldsymbol{u}_{MPCref,k}$ are the reference control inputs which are obtained based on the equilibrium point corresponding to the target position. The cost function is thus designed to correct any deviation

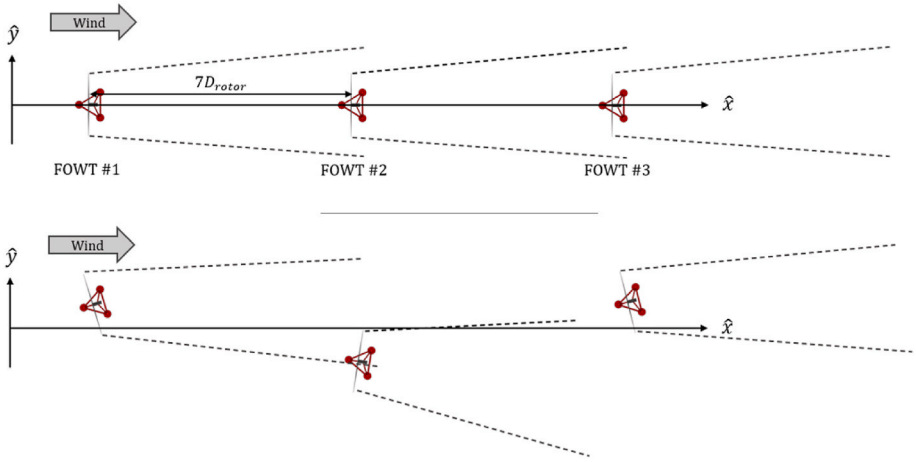

Fig. 7. Initial floating wind farm configuration for the first and second control scenarios (upper) and schematic representation of the repositioning process (lower).

between the wind turbine's actual position and its target position, while simultaneously ensuring safe operation through generator speed regulation (to prevent full stall and turbine shutdown) and controlled management of inputs. This is achieved by a key feature of the MPC control scheme, which imposes constraints on the control law at each time step k to enforce compliance with saturation and rate limits for control inputs (as shown in Table 2), along with other possible constraints, such as permissible horizontal displacements, generator rotational speeds, and platform rotations (Jard and Snaiki, 2023; Jonkman et al., 2009).

4. Case study

The primary objective of this section is to develop a control strategy for optimizing floating wind turbine performance. However, before implementing control algorithms, it's important to perform sensitivity analyses on both the wake model and the wind turbine model. This analysis will assess the robustness of these models to variations in key parameters and environmental conditions. The results of the sensitivity analysis are summarized in the Appendix. To demonstrate the performance of the proposed control strategy for floating wind turbines under varying wind conditions, three distinct case scenarios will be analyzed using the dynamic wind farm model (FOWFSim-Dyn) and Matlab/Simulink. In the first scenario, the focus is on maximizing power production, whereas the second scenario involves a specified target power output. A final scenario was conducted to assess the control strategy's adaptability to a randomly initialized layout. The first two scenarios involve a 1x3 wind farm layout with 5 MW FOWTs, initially aligned in the wind direction ($\hat{x}$) and separated by a distance equivalent to seven times the diameter of their rotor. Fig. 7 depicts the wind farm configuration and illustrates the repositioning process.

Each FOWT is equipped with an MPC controller, which receives instructions from the centralized wind farm controller. To extend the movable range of the platform, the mooring cables for each floating platform have been adjusted to a length of 920 [m], compared to the initial length of 835.5 [m]. This modification is a common practice in studies involving floating turbine repositioning, as the standard cable length excessively limits the movable range (Kheirabadi and Nagamune, 2019; Gao et al., 2022; Han et al., 2017). Here, a length of 920 [m] was selected to achieve a range of motion that meets the requirements of this study (Kheirabadi and Nagamune, 2019). It should be noted that the longitudinal platform position (x_i) is not actively controlled in this application due to its minimal variation (Kheirabadi and Nagamune, 2019). Therefore, it does not affect significantly the power production, unlike the lateral platform position (y_i). However, constraints are still applied to the longitudinal platform position x_i to ensure a stable and safe operation of the system. Furthermore, while the FOWFSim-Dyn model has the capability to accommodate fluctuating wind conditions over time, it only considers a calm sea state without waves as the basis of its operation (Kheirabadi and Nagamune, 2021b), therefore the waves were not considered in this study. As a result, the linearized model of the MPC controller was developed solely based on wind speed. Nevertheless, it's worth noting that the suggested controller has the capability to incorporate both wind and wave disturbances with minimal adjustments to the control parameters. In all scenarios, the wind conditions were determined for a 1-h duration using the Von Karman turbulence spectrum, where the mean incident wind speed at the rotor hub height was set at $\overline{\mathbf{V}}_{\infty} = [14, 0]$ [m/s], with a turbulent intensity of 0.036 and an integral length scale of 170 [m]. It is important to emphasize that when wind speeds are excessively low, the repositioning mechanism, which relies on directly manipulating the aerodynamic thrust force, may not be effective. In fact, during periods of low wind speeds, the thrust force might be too weak to compensate the effects of other forces, such as those from the mooring lines. Consequently, specific repositioning tasks related to power demand may not be achievable. To address these challenges, potential solutions include increasing the length of the mooring lines to reduce the magnitude of the restoring force or incorporating additional actuators to aid in repositioning the wind turbine under such conditions (Gao et al., 2022; Escobar Aquino and Nagamune, 2020; Niu et al., 2023; Han et al., 2017).

To maintain the wind turbine within its designated operating range (Jonkman et al., 2009), a series of constraints must be enforced. This involves imposing restrictions on the generator's rotational speed, ω_g, to ensure it falls within the range of 669.3 [rpm] to 1173.7 [rpm]. Additionally, saturation and rate-limits on control inputs, as outlined in Table (2), are enforced. It's important to highlight that a maximum value for the collective blade pitch angle, β_i, is set at 0°. This decision is made to prevent any value above 0°, which could potentially occur at lower wind speeds. Exceeding this value would trigger a shift in the control logic from pitch-to-stall regulation to pitch-to-feather regulation. This nonlinear transition can lead to instability in the operation of the wind turbine and result in inappropriate control responses as the controller relies on a linear prediction model.

The predictive models associated with the MPC controllers were linearized at multiple equilibrium points, including both the initial and target positions. These positions are determined by the centralized wind farm controller based on the selected scenario. Subsequently, the wind turbine controller will transition from one equilibrium point to another in accordance with the designated target position. The MPC parameters, such as prediction and control horizons as well as weight matrices, were determined through a trial-and-error process. Initially, the FOWTs are oriented along the $\hat{x}$-axis with starting positions of $(x_1, x_2, x_3) = (84, 966, 1848)$ [m] and $(y_1, y_2, y_3) = (0, 0, 0)$ [m]. The mean power

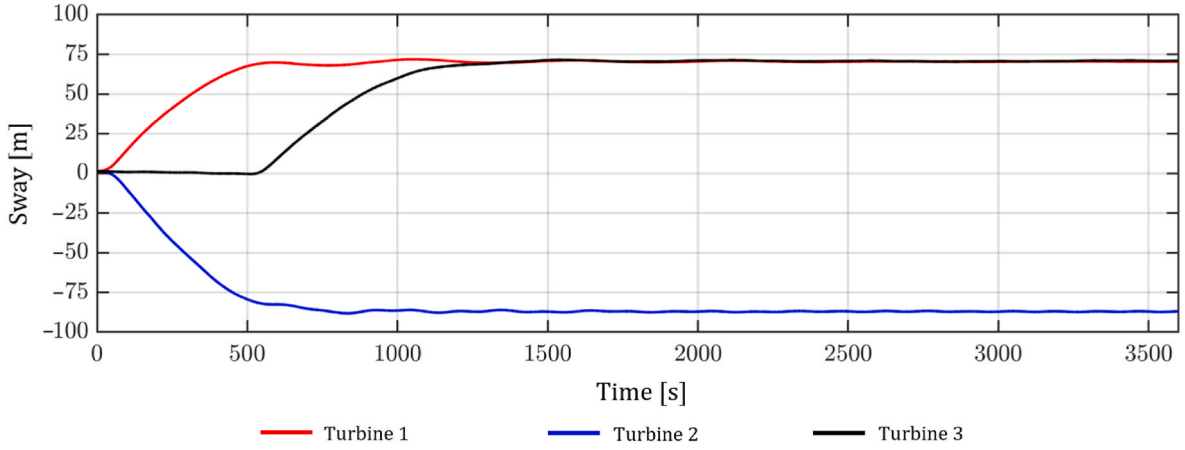

Fig. 8. Crosswind platform displacements under the 1st control scenario.

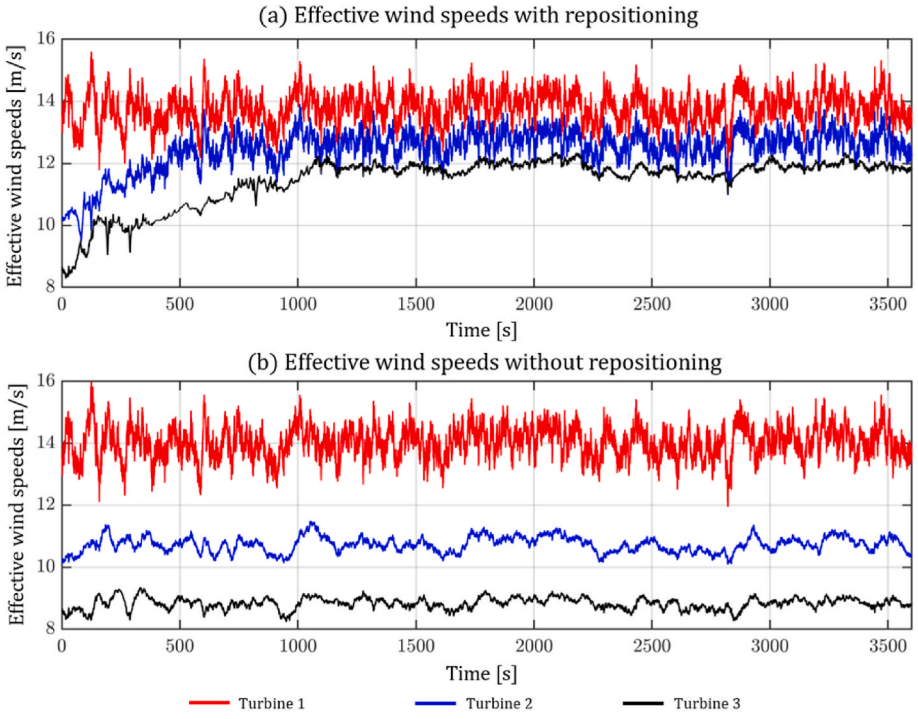

Fig. 9. Time series of the effective wind speeds experienced by each FOWT for the 1st control scenario under two conditions: (a) with repositioning and (b) without repositioning.

output is $(P_{out,1}, P_{out,2}, P_{out,3}) = (5, 3, 3)$[MW], clearly indicating the substantial impact of wake effects, particularly on the downstream wind turbines.

4.1. First scenario

In this scenario, the primary objective is to maximize the total power output from the wind farm, denoted as P_{farm} (Eq. (11)). This goal must be achieved while adhering to system constraints and mitigating the impact of wake effects. Consequently, the centralized wind farm controller's task is to determine the optimal positions for each wind turbine, specifically their lateral positions defined by their respective yaw angles. Subsequently, the wind turbine controllers are tasked to achieve the prescribed targets. An alternative approach to formulating the optimization problem is to instruct the centralized controller to determine optimal turbine locations by maximizing the sum of the effective wind velocity projected onto the rotor-swept area $V_{\perp,i}$ of each turbine i. Details of the solution to this optimization problem and the performance of the wind turbine control system are provided in Sect. 4.1.1, 4.1.2 and 4.1.3.

4.1.1. Position control results

The resulting target lateral positions for the 1st, 2nd and 3rd wind turbines were 72, -89, and 70 [m], respectively. The time series of the lateral positions (i.e., sways), using the individual MPC controllers, are illustrated in Fig. 8. It can be concluded that the MPC controllers have effectively and promptly adjusted the lateral positions of the wind turbines to align with their designated target values. Specifically, the target positions were attained within 580 [s] for the 1st, 830 [s] for the 2nd, and 835 [s] for the 3rd wind turbine. These positions were then consistently maintained until the end of the scenario. The obtained root mean square error (RMSE) with respect to the target positions for the lateral displacement were 1.82 [m], 1.97 [m], and 0.85 [m], for the 1st, 2nd and 3rd wind turbines respectively. These results underline the

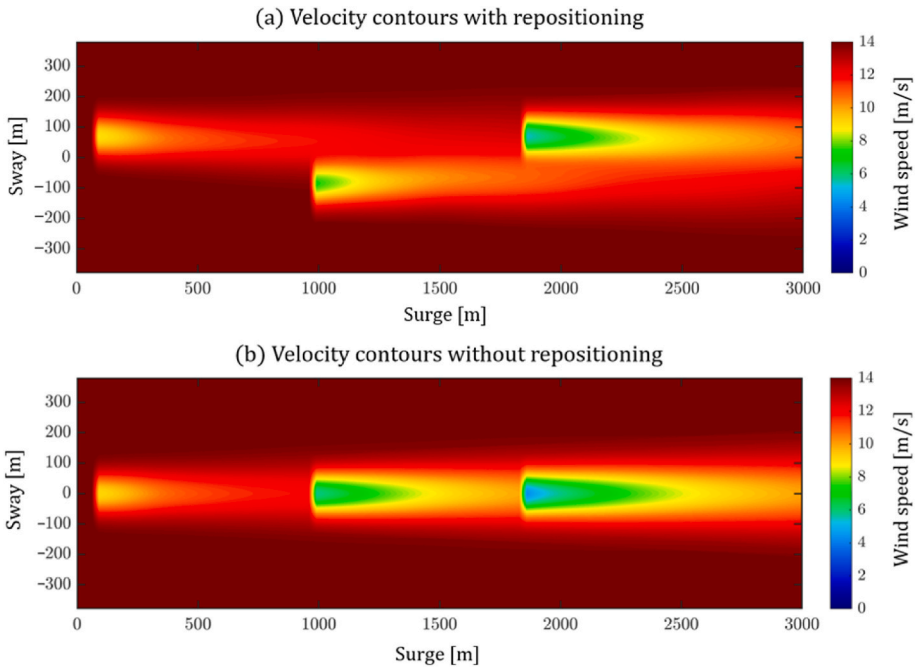

Fig. 10. Velocity contour plots at time step $t = 3500$ [s] for the 1st control scenario under two conditions: (a) with repositioning and (b) without repositioning.

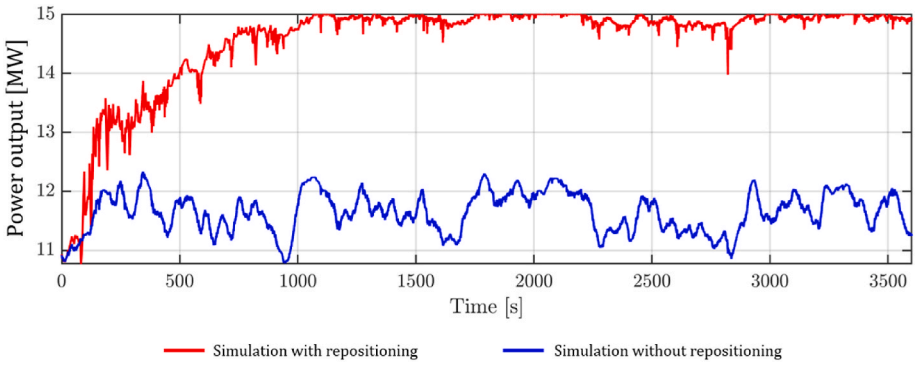

Fig. 11. Time series of the wind farm total power output for the 1st control scenario under two conditions: with repositioning (red) and without repositioning (blue). (For interpretation of the references to colour in this figure legend, the reader is referred to the Web version of this article.)

controllers' remarkable accuracy in achieving the desired positions. It's worth noting that a deliberate delay of 500 [s] (determined through trial and error) was introduced for the 3rd turbine to ensure smooth repositioning and avoid potential issues, such as complete aerodynamic stall or turbine shutdown, during periods of low wind speeds.

4.1.2. Power control results

To evaluate the performance of the wind farm controller, it will be compared to a wind farm without a repositioning mechanism, where the turbines are kept at their initial starting positions. The time series of the effective wind speeds experienced by each turbine (i.e., $V_{\perp_i}$) are plotted in Fig. 9 for both scenarios.

It can be concluded that the wind turbine repositioning mechanism plays a substantial role in mitigating wake effects, as the effective wind speeds perceived by downstream turbines are significantly higher compared to a scenario without repositioning. Specifically, after the repositioning of each wind turbine (starting from 1335 [s]), the average effective wind speeds perceived by the 2nd and 3rd downstream turbines have increased by 17.88% and 34.16%, respectively. Furthermore, there is a slight reduction in the effective wind speed perceived by the upstream turbine, which can be attributed to the nacelle misalignment, necessary for platform repositioning. While this misalignment does marginally decrease the perceived wind speed, the impact on power production remains negligible.

To highlight the significant impact of the wake effects, the velocity contour plots at the end of the platform repositioning (i.e., at time $t = 3500$ [s]) are plotted in Fig. 10. It can be concluded that, unlike the scenario without repositioning, the proposed control strategy has successfully relocated the platforms to avoid the wake regions and hence increase the perceived wind speeds which will ultimately maximize the power generation. By avoiding the wake regions, which are characterized by reduced wind speeds and significant fatigue loads, both the power production and service life can be increased.

Similar to the perceived FOWT wind speeds, the total power output of the wind farm has also reached its peak value (~ 15 [MW]) as depicted in Fig. 11. Specifically, the repositioning of the platforms has led to a remarkable 25.05% increase in energy production over the course of 1 h compared to a scenario where repositioning was not employed. This substantial gain outperforms many existing control-based strategies aimed at mitigating wake effects (Steinbuch et al., 1988; Fleming et al., 2015).

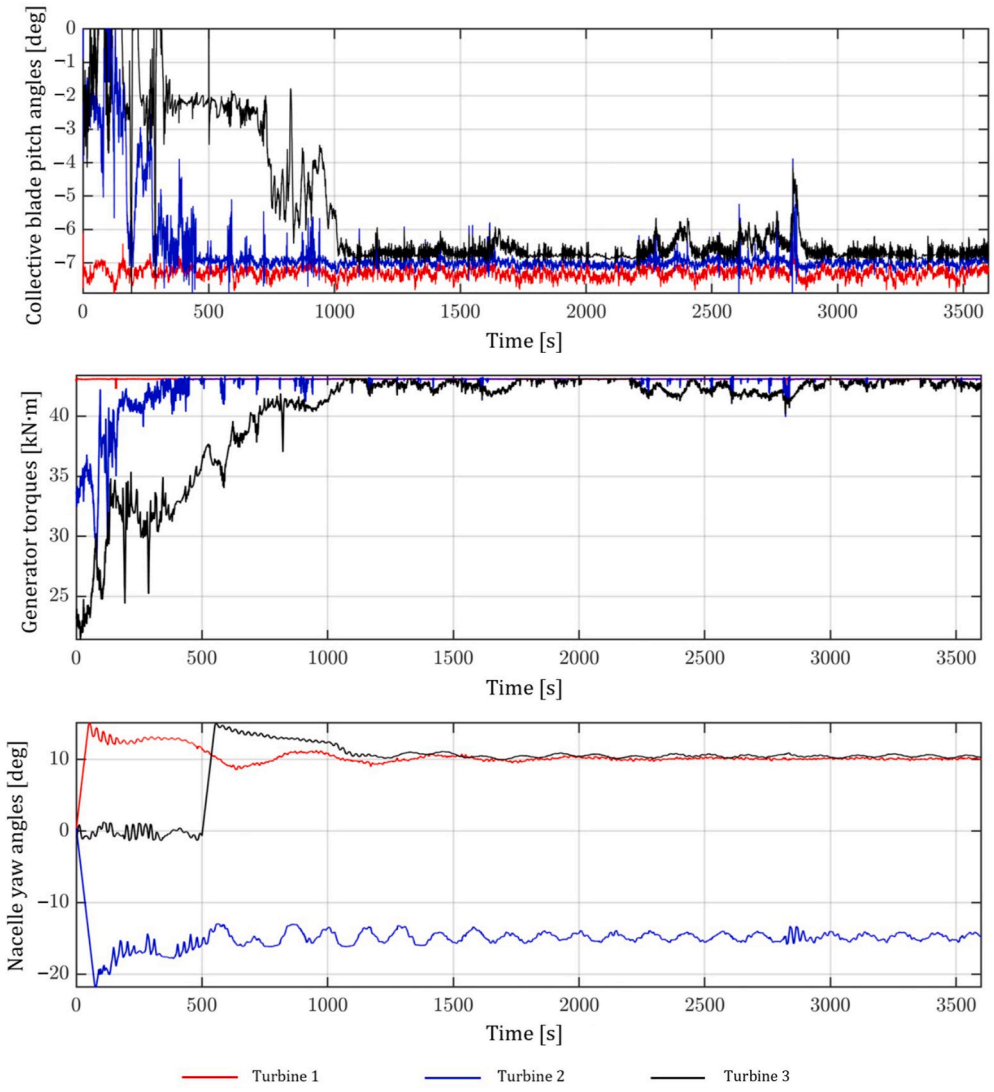

Fig. 12. Time series of the control inputs for the 1st control scenario.

4.1.3. Control inputs results

The time series representations of the control inputs for the three MPC controllers are presented in Fig. 12. It can be concluded that all control inputs have remained within the prescribed safety limits while adhering to the constraints detailed in Table 2. In addition, the nacelle yaw angles exhibit a comparable trend to that of the crosswind platform displacements. The MPC controllers have swiftly adapted all control inputs to effectively address the control scenario. Clearly, the 3rd wind turbine required additional time to adapt its control inputs due to the imposed delay (i.e., 500 [s]). Moreover, owing to the initially low wind speeds experienced by the downstream turbines during the early stages of the simulation, the collective blade pitch angles approached values close to zero degrees. This adjustment was made to prevent stall and optimize wind energy extraction under these specific conditions. As previously mentioned, a strict upper limit of 0° has been imposed on the collective blade pitch angle. Exceeding this threshold triggers a

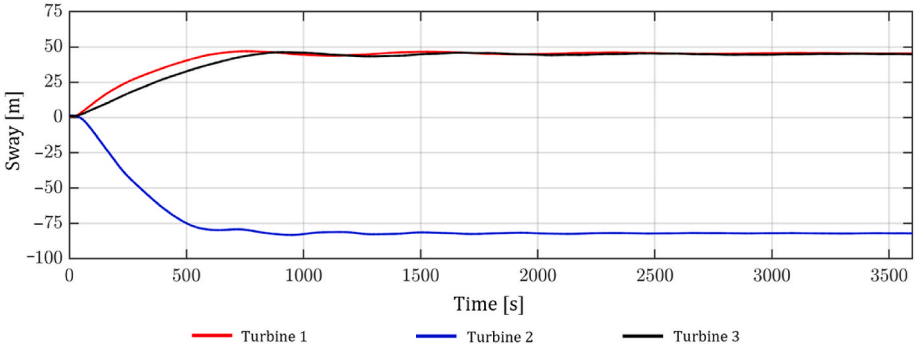

Fig. 13. Crosswind platform displacements under the 2nd control scenario.

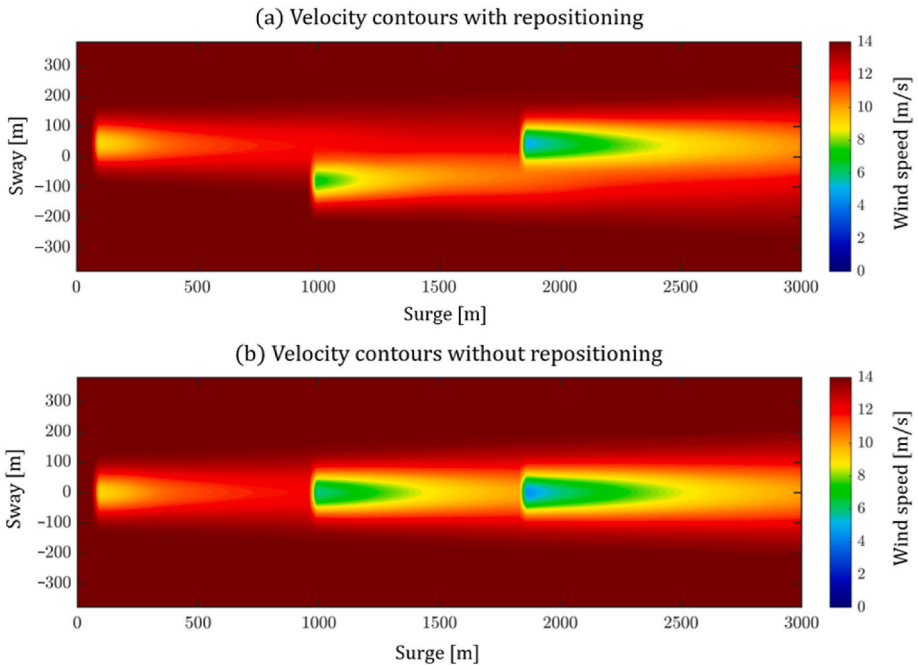

Fig. 14. Velocity contour plots at time step $t = 3500$ [s] for the 2nd control scenario under two conditions: (a) with repositioning and (b) without repositioning.

transition in the control logic from pitch-to-stall regulation to pitch-to-feather regulation that cannot be properly managed by the controller. As the perceived wind speeds for the downstream turbines increase, the collective blade pitch angles stabilize at values below zero degrees. This adjustment is made to prevent excessive kinetic energy extraction from the wind through aerodynamic stall. It also facilitates the platform repositioning process while aligning with the power production target.

4.2. Second scenario

In this particular scenario, the wind farm is required to achieve a target total power output of $P_{farm,tar} = 13$ [MW], representing a realistic power demand from the electrical grid. Additionally, the control strategy must operate within the system constraints while addressing wake effects mitigation. Furthermore, the optimization problem will prioritize minimizing yaw angles to discourage substantial displacements while evading wake regions. All other constraints and system parameters remain consistent with the previous scenario. It's worth noting that, unlike the first scenario, the imposed delay for the 3rd wind turbine has been eliminated. In the subsequent sections, only the results related to position, velocity contours, and power will be presented, as the overall system behavior remains largely consistent with the previous case.

4.2.1. Position control results

The target lateral positions achieved were 45, -82, and 45 [m] for the 1st, 2nd and 3rd wind turbines, respectively. Fig. 13 illustrates the time series of these lateral positions. In this scenario as well, each wind turbine platform successfully reached and maintained its designated position target as instructed by the centralized wind farm controller. These position targets were attained after 630 [s], 840 [s], and 820 [s], respectively, and remained stable until the end of the simulation. The RMSE values for the 1st, 2nd and 3rd wind turbine platforms were 0.85 [m], 0.37 [m], and 0.64 [m], respectively. It's worth mentioning that the relatively observed lower errors can be attributed to the controllers finding it comparatively easier to reach and maintain these positions. This ease is primarily because these positions are in close proximity to the wind turbines' initial locations, requiring minimal rotor misalignment. In addition, no delay was required for this scenario, as the 3rd wind turbine was able to achieve and maintain its final position without any observed operational instability.

4.2.2. Power control results

Just as in the 1st scenario, velocity contour plots are provided in Fig. 14 at the end of the platform repositioning (i.e., at time $t = 3500$ [s]) for both the repositioning and non-repositioning cases. It can be concluded that the control strategy has successfully relocated the

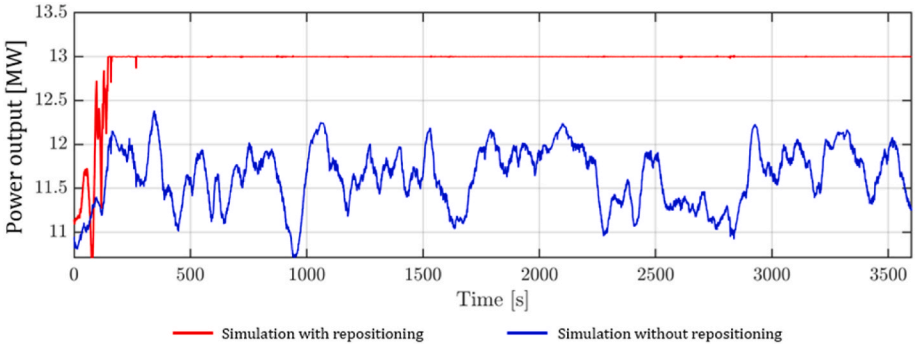

Fig. 15. Time series of the wind farm total power output for the 2nd control scenario under two conditions: with repositioning (red) and without repositioning (blue). (For interpretation of the references to colour in this figure legend, the reader is referred to the Web version of this article.)

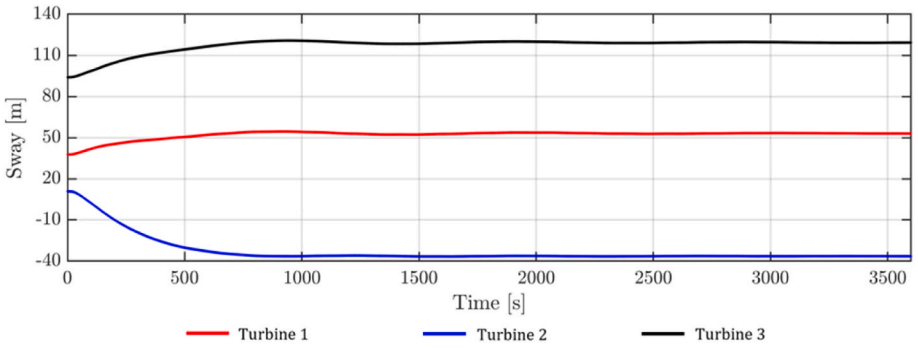

Fig. 16. Crosswind platform displacements under the 3rd control scenario.

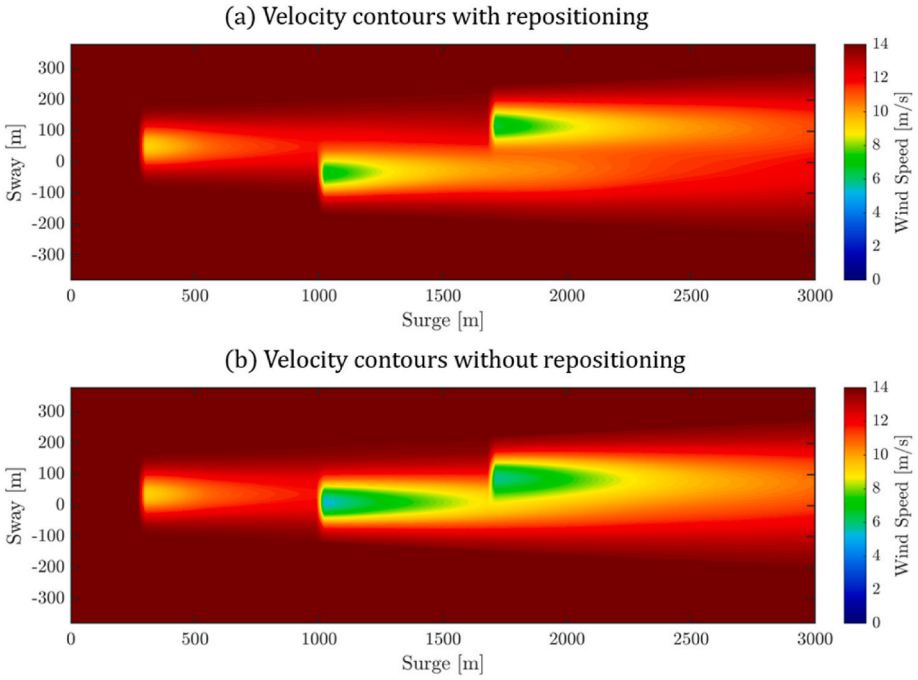

Fig. 17. Velocity contour plots at time step $t = 3500$ [s] for the 3rd control scenario under two conditions: (a) with repositioning and (b) without repositioning.

platforms, avoiding wake-prone regions to alleviate fatigue loads while satisfying the control objectives and constraints.

The wind farm's total power production has successfully achieved its specified target of ~ 13 [MW], as shown by the power generation time series depicted in Fig. 15. In contrast, the scenario without repositioning failed to reach the 13 [MW] target at any point. Furthermore, the power generation in the repositioning scenario demonstrated increased stability, enhancing its suitability and reliability for meeting the requested power demand from the electrical grid.

4.3. Third scenario

To assess the control process's adaptability, the initial 1x3 wind farm layout was modified. The turbines' neutral positions and anchor points

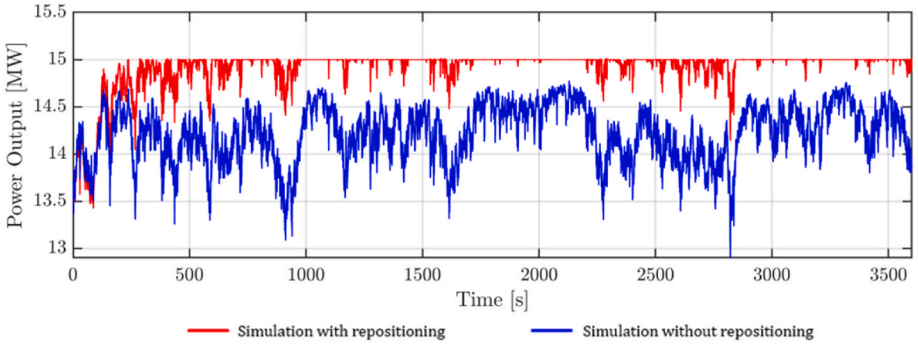

Fig. 18. Time series of the wind farm total power output for the 3rd control scenario under two conditions: with repositioning (red) and without repositioning (blue). (For interpretation of the references to colour in this figure legend, the reader is referred to the Web version of this article.)

were randomly shifted to represent a new configuration. The FOWTs are now located at $(x_1, x_2, x_3) = (195, 920, 1600)$ [m] and $(y_1, y_2, y_3) = (37, 10, 93)$ [m]. For this scenario, the wind farm controller's objective is to maximize the total power output of the wind farm P_{farm} (Eq. (11)), while maintaining the same constraints and other system parameters as in the first scenario.

4.3.1. Position control results

The optimal lateral target positions determined by the wind farm controller are 53, -37, and 119 [m] for the 1st, 2nd, and 3rd turbines, respectively. Fig. 16 illustrates the time series of these lateral positions. Each floating platform was able to reach its final position and maintain stability until the end of the simulation, despite the new wind farm layout. The target positions were reached after 660, 700, and 790 [s], with RMSE errors of 0.56, 0.60, and 0.73 [m], respectively. It's important to note that no delay in applying the target positions was necessary for the 3rd turbine due to the minimal displacement required. Additionally, no instability was observed during the operation.

4.3.2. Power control results

The velocity contours are plotted in Fig. 17 at time t = 3500 [s]. As illustrated, without repositioning, the velocity deficit behind the second turbine is significantly greater than in the first scenario. This is attributed to the shorter longitudinal distance between the turbines compared to the first scenario (less than 7 diameters, which is typically the recommended distance by wind farm designers), resulting in a less dissipated wake downstream. Importantly, the proposed control framework effectively mitigates these wake effects by repositioning the platforms, leading to a positive impact on power production.

The corresponding power output is shown in Fig. 18. The repositioning strategy has resulted in a 5% increase in the wind farm's power production over 1 h, while also significantly reducing the presence of turbines within the wake of others. Although the power gain is smaller compared to previous scenarios, this can be attributed to the initial layout, which was already relatively favorable as the turbines were not directly aligned with the wind direction. In this specific case, while the second turbine's output is lower due to the reduced longitudinal spacing, the third turbine's output is significantly higher due to its advantageous initial position, leading to smaller overall power losses. Despite the smaller power gain, the repositioning strategy remains valuable due to its drastic reduction in wake-related interactions and its demonstrated flexibility across different wind farm layouts.

5. Conclusion

In this study, the dynamic layout optimization approach for offshore floating wind farms was investigated to meet power requirements and alleviate wake effects. Three scenarios were considered: two of them prioritized power maximization over different layouts configurations, while the other focused on power set-point tracking. The initial step of the proposed control methodology involved a centralized wind farm controller tasked with identifying the optimal wind farm layout to fulfill power requirements while effectively mitigating wake effects. This optimization process was executed using Matlab/Simulink. Subsequently, wind turbine controllers were asked to achieve the specified objectives. Each Floating Offshore Wind Turbine (FOWT) was equipped with a Model Predictive Control (MPC) system, which directly manipulated the aerodynamic thrust force through three control inputs: collective blade pitch angle, generator torque, and nacelle yaw angle. The proposed control strategy integrated an efficient dynamic wind farm model, which simulates the floating platform motion and wake transport under varying wind conditions. Furthermore, the MPC predictive model was based on a highly efficient dynamic model specifically designed for real-time control applications. To highlight the effectiveness of the proposed approach, a case study was conducted using a 1x3 layout wind farm configuration. Both power maximization and regulation scenarios were evaluated using 5 MW offshore semi-submersible baseline wind turbines. The obtained results demonstrate the successful repositioning of wind turbines in both scenarios with low root mean square errors, effectively avoiding wake regions. This achievement resulted in a remarkable 25% enhancement in stable energy production when compared to a static layout configuration within a 1-h timeframe for the first control scenario. Moreover, in the second scenario, the intended power production was promptly achieved and consistently sustained throughout the control scenario. In the final scenario, the control strategy's adaptability to various wind farm layouts was demonstrated. Due to its reliable control performance and rapid response time, the proposed control approach can be conveniently integrated into both new and existing floating wind farms without requiring any extra hardware.

CRediT authorship contribution statement

Timothé Jard: Writing – review & editing, Writing – original draft, Visualization, Validation, Software, Methodology, Investigation, Formal analysis, Data curation, Conceptualization. **Reda Snaiki:** Writing – review & editing, Writing – original draft, Supervision, Resources, Project administration, Methodology, Investigation, Funding acquisition, Formal analysis, Conceptualization.

Declaration of competing interest

The authors declare that they have no known competing financial interests or personal relationships that could have appeared to influence the work reported in this paper.

Acknowledgements

This work was partly supported by the Natural Sciences and Engineering Research Council of Canada (NSERC) [grant number CRSNG RGPIN 2022-03492].

Appendix. Sensitivity analysis

To assess the robustness of the wake model (FOWFSim-Dyn) and wind turbine model to varying conditions, a sensitivity analysis is conducted. A baseline scenario is established for the first sensitivity analysis with γ (yaw angle) set to 0 [deg], U_∞ (freestream wind speed) at 14 [m/s], and V_∞ (perpendicular wind component) at 0 [m/s]. Table 3 details the results of the sensitivity analysis for the FOWFSim-Dyn model.

Table 3
Sensitivity analysis of the wake model

Input parameter	Value	y_w[m]		$v_{w,x}$[m/s]		$v_{w,y}$[m/s]		D_w[m]	
		$4D_{rotor}$	$5D_{rotor}$	$4D_{rotor}$	$5D_{rotor}$	$4D_{rotor}$	$5D_{rotor}$	$4D_{rotor}$	$5D_{rotor}$
γ [deg]	−10	7.38	8.82	12.49	12.66	0.19	0.17	166.3	176.4
	−5	3.81	4.55	12.49	12.65	0.10	0.08	166.3	176.4
	0	0	0	12.48	12.65	0	0	166.3	176.4
	5	−3.81	−4.55	12.49	12.65	−0.10	−0.08	166.3	176.4
	10	−7.38	−8.82	12.49	12.66	−0.19	−0.17	166.3	176.4
U_∞ [m/s]	14	0	0	12.48	12.65	0	0	166.3	176.4
	16	0	0	14.15	14.33	0	0	161.3	170.1
	18	0	0	15.89	16.09	0	0	157.4	165.2
	20	0	0	17.72	17.91	0	0	157.3	161.3
	22	0	0	19.69	19.87	0	0	151.7	158.2
V_∞ [m/s]	−4	−137.9	−171.9	12.4	12.57	−3.85	−3.86	166.3	176.4
	−2	−69.59	−86.7	12.46	12.63	−1.94	−1.94	166.3	176.4
	0	0	0	12.48	12.65	0	0	166.3	176.4
	2	69.59	86.7	12.46	12.63	1.94	1.94	166.3	176.4
	4	137.9	171.9	12.4	12.57	3.85	3.86	166.3	176.4

The simulations show that yaw angle (γ) strongly influences wake deflection (y_w), with higher yaw angles leading to greater deflection at different downstream locations (e.g., 8.82 [m] for $\gamma = -10$ [deg] compared to 4.55 [m] for $\gamma = -5$ [deg] at $5D_{rotor}$ downstream distance). Interestingly, yaw angle seems to have minimal impact on wake diameter (D_w) or centerline wake velocity in the streamwise direction ($v_{w,x}$). Freestream wind speed (U_∞) primarily affects $v_{w,x}$ (increasing from 12.65 [m/s] to 19.87 [m/s] with U_∞ going from 14 [m/s] to 22 [m/s] at $5D_{rotor}$ downstream distance), while also causing a decrease in wake diameter (D_w) with a nearly 10% reduction from 176.4 [m] to 158.2 [m] as U_∞ increases from 14 [m/s] to 22 [m/s]. Finally, the perpendicular wind component (V_∞) significantly impacts wake deflection and vertical wake velocity ($v_{w,y}$) with minimal influence on other variables.

To assess the internal wind turbine model within the MPC controller, a separate sensitivity analysis was conducted (detailed in Table 4). This analysis examines the model's response to variations in key parameters from a baseline scenario of: $\beta = 8$ [deg], $\tau_g = 25000$ [Nm], $\gamma = 0$ [deg], cable length = 835.5 [m], $U_\infty = 14$ [m/s], and wave height = 0 [m]. Notably, Table 4 only reports the final values obtained after a 1000-s simulation without any control intervention.

Table 4
Sensitivity analysis of the wake model

Input parameter	Values	Surge x [m]	Sway y [m]	Roll θ_x [deg]	Pitch θ_y [deg]	Yaw θ_z [deg]
β [deg]	6	7.5	0	0.49	3.09	−0.18
	7	7	0	0.48	2.8	−0.19
	8	6.2	0	0.48	2.5	−0.21
	9	5.5	0	0.47	2.19	−0.22
	10	4.8	0	0.46	1.87	−0.22
τ_g [Nm]	20000	6.2	0	0.40	2.5	−0.17
	22500	6.2	0	0.44	2.5	−0.19
	25000	6.2	0	0.48	2.5	−0.21
	27500	6.2	0	0.51	2.5	−0.22
	30000	6.2	0	0.55	2.5	−0.24
γ [deg]	−10	6	−1.35	0.90	2.29	−0.24
	−5	6.1	−0.6	0.70	2.43	−0.22
	0	6.2	0	0.48	2.5	−0.21
	5	6.1	0.6	0.26	2.52	−0.19
	10	6	1.35	0.05	2.48	−0.17
Cable length [m]	825	3	0	0.38	2.44	−0.16
	830	4.5	0	0.32	2.49	−0.16
	835.5	6.2	0	0.48	2.5	−0.21
	840	8	0	0.22	2.51	−0.29
	845	11	0	0.19	2.52	−0.43
U_∞ [m/s]	14	6.2	0	0.48	2.5	−0.21
	16	8	0	0.49	3.25	−0.18
	18	9.5	0	0.49	3.98	−0.19
	20	10.5	0	0.49	4.62	−0.22
	22	11	0	0.47	4.99	−0.21
Wave height [m]	0	6.2	0	0.48	2.5	−0.21
	1	6.2	0	0.35	2.63	−0.24
	2	6	0	0.35	2.74	−0.25
	3	6	0	0.34	2.84	−0.25
	4	6	0	0.34	2.92	−0.25

The simulations reveal that pitch angle (β) primarily controls surge displacement (increasing values lead to greater surge, e.g., 7.5 [m] for $\beta = 6$ [deg] compared to 4.8 [m] for $\beta = 10$ [deg]), while also significantly reducing pitch angle (θ_y) as β increases (e.g., θ_y decreases from 3.09 [deg] to

1.87 [deg] for $\beta = 6$ [deg] to 10 [deg]). While yaw angle (γ) mainly influences sway displacement (y), with larger yaw angles causing greater sway (e.g., 1.35 [m] for $\gamma = 10$ [deg] compared to 0.6 [m] for $\gamma = 5$ [deg]), it has minimal impact on surge. Table 4 suggests yaw angle also affects other rotational motions like roll. In addition, it can be concluded that the cable length has significant influence on the platform displacement. Longer cables lead to increased surge displacement (e.g., surge rose from 3 [m] to 11 [m] when cable length went from 825 [m] to 845 [m]) and larger pitch and yaw rotations. The analysis also revealed that generator torque (τ_g) primarily influences roll (θ_x) and yaw (θ_z). For example, a roll angle of 0.4 [deg] was observed with a generator torque of 20000 [Nm], compared to 0.55 [deg] at 30000 Nm. Among the environmental factors, freestream wind speed (U_∞) mainly affects surge and pitch, while wave height has the strongest impact on the rotational degrees of freedom. The sensitivity analysis reinforces the importance of the proposed control inputs (yaw angle, collective blade pitch angle, and generator torque) for optimizing wind turbine performance. By strategically adjusting these inputs, the thrust force can be manipulated without introducing additional complex machinery (actuators) to the system. This simplifies the design and potentially reduces maintenance costs while achieving the desired control of the turbine and wind farm.

References

Annoni, J., Gebraad, P.M.O., Scholbrock, A.K., Fleming, P.A., Wingerden, J.V., 2016. Analysis of axial-induction-based wind plant control using an engineering and a high-order wind plant model. Wind Energy 19, 1135–1150. https://doi.org/10.1002/we.1891.

Barthelmie, R.J., Hansen, K., Frandsen, S.T., Rathmann, O., Schepers, J.G., Schlez, W., Phillips, J., Rados, K., Zervos, A., Politis, E.S., et al., 2009. Modelling and measuring flow and wind turbine wakes in Large wind farms offshore. Wind Energy 12, 431–444. https://doi.org/10.1002/we.348.

Bastankhah, M., Porté-Agel, F., 2016. Experimental and theoretical study of wind turbine wakes in yawed conditions. J. Fluid Mech. 806, 506–541. https://doi.org/10.1017/jfm.2016.595.

Bastankhah, M., Porté-Agel, F., 2019. Wind farm power optimization via yaw angle control: a wind tunnel study. J. Renew. Sustain. Energy 11, 023301. https://doi.org/10.1063/1.5077038.

Bitar, E., Seiler, P., 2013. Coordinated control of a wind turbine array for power maximization. In: Proceedings of the 2013 American Control Conference. IEEE, Washington, DC, pp. 2898–2904.

Boersma, S., Doekemeijer, B.M., Gebraad, P.M.O., Fleming, P., Annoni, J., Scholbrock, A. K., Frederik, J.A., van Wingerden, J.-W., 2017. A tutorial on control-oriented modeling and control of wind farms. In: Proceedings of the 2017 American Control Conference (ACC). IEEE, Seattle, WA, USA, pp. 1–18.

Burton, T., Jenkins, N., Sharpe, D., Bossanyi, E., 2011. Wind Energy Handbook, first ed. Wiley. ISBN 978-0-470-69975-1.

Escobar Aquino, E.E., Nagamune, R., 2020. H∞ position transfer and regulation for floating offshore wind turbines. Control Theory Technol 18, 231–245. https://doi.org/10.1007/s11768-020-8280-9.

Fleming, P., Gebraad, P.M.O., Lee, S., van Wingerden, J.-W., Johnson, K., Churchfield, M., Michalakes, J., Spalart, P., Moriarty, P., 2014. Evaluating techniques for redirecting turbine wakes using SOWFA. Renew. Energy 70, 211–218. https://doi.org/10.1016/j.renene.2014.02.015.

Fleming, P., Gebraad, P.M.O., Lee, S., van Wingerden, J.-W., Johnson, K., Churchfield, M., Michalakes, J., Spalart, P., Moriarty, P., 2015. Simulation comparison of wake mitigation control strategies for a two-turbine case. Wind Energy 18, 2135–2143. https://doi.org/10.1002/we.1810.

Gao, Y., Padmanabhan, A., Chen, O., Kheirabadi, A.C., Nagamune, R., 2022. A baseline repositioning controller for a floating offshore wind farm. In: Proceedings of the 2022 American Control Conference (ACC). IEEE, Atlanta, GA, USA, pp. 4224–4229.

Gebraad, P.M.O., Teeuwisse, F.W., van Wingerden, J.W., Fleming, P., Ruben, S.D., Marden, J.R., Pao, L.Y., 2016. Wind plant power optimization through yaw control using a parametric model for wake effects-a CFD simulation study: wind plant optimization by yaw control using a parametric wake model. Wind Energy 19, 95–114. https://doi.org/10.1002/we.1822.

Gonzalez, J.S., Payan, M.B., Santos, J.R., 2013. Optimal control of wind turbines for minimizing overall wake effect losses in offshore wind farms. In: Proceedings of the Eurocon 2013. IEEE, Zagreb, Croatia, pp. 1129–1134.

Guntur, S., Troldborg, N., Gaunaa, M., 2012. Application of engineering models to predict wake deflection due to a tilted wind turbine. Presented at the EWEC 2012 - European Wind Energy Conference & Exhibition, Copenhagen, Denmark.

Han, C., Nagamune, R., 2020. Platform position control of floating wind turbines using aerodynamic force. Renew. Energy 151, 896–907. https://doi.org/10.1016/j.renene.2019.11.079.

Han, C., Homer, J.R., Nagamune, R., 2017. Movable range and position control of an offshore wind turbine with a semi-submersible floating platform. In: Proceedings of the 2017 American Control Conference (ACC). IEEE, Seattle, WA, USA, pp. 1389–1394.

Homer, J.R., Nagamune, R., 2018. Physics-based 3-D control-oriented modeling of floating wind turbines. IEEE Trans. Control Syst. Technol. 26, 14–26. https://doi.org/10.1109/TCST.2017.2654420.

Jahangiri, V., Sun, C., 2020. Three-dimensional vibration control of offshore floating wind turbines using multiple tuned mass dampers. Ocean Eng 206, 107196. https://doi.org/10.1016/j.oceaneng.2020.107196.

Jahangiri, V., Sun, C., 2022. A novel three dimensional nonlinear tuned mass damper and its application in floating offshore wind turbines. Ocean Eng 250, 110703. https://doi.org/10.1016/j.oceaneng.2022.110703.

Jard, T., Snaiki, R., 2023. Real-time repositioning of floating wind turbines using model predictive control for position and power regulation. Wind 3, 131–150. https://doi.org/10.3390/wind3020009.

Jiménez, Á., Crespo, A., Migoya, E., 2009. Application of a LES technique to characterize the wake deflection of a wind turbine in yaw. Wind Energy 13, 559–572. https://doi.org/10.1002/we.380.

Johnson, K.E., Thomas, N., 2009. Wind farm control: addressing the aerodynamic interaction among wind turbines. In: Proceedings of the 2009 American Control Conference. IEEE, St. Louis, MO, USA, pp. 2104–2109.

Jonkman, J., 2009. Dynamics of offshore floating wind turbines-model development and verification. Wind Energy 12, 459–492. https://doi.org/10.1002/we.347.

Jonkman, J., Butterfield, S., Musial, W., Scott, G., 2009. Definition of a 5-MW Reference Wind Turbine for Offshore System Development. National Renewable Energy Laboratory, Golden, CO, USA, 947422. NREL/TP-500-38060.

Katic, I., Højstrup, J., Jensen, N.O., 1987. A simple model for cluster efficiency. In: Palz, W., Sesto, E., Raguzzi, A. (Eds.), European Wind Energy Association Conference and Exhibition: EWEC'86. Proceedings, vol. 1, pp. 407–410. Rome, Italy.

Kheirabadi, A.C., Nagamune, R., 2019. Modeling and power optimization of floating offshore wind farms with yaw and induction-based turbine repositioning. In: Proceedings of the 2019 American Control Conference (ACC). IEEE, Philadelphia, PA, USA, pp. 5458–5463.

Kheirabadi, A.C., Nagamune, R., 2020. Real-time relocation of floating offshore wind turbine platforms for wind farm efficiency maximization: an assessment of feasibility and steady-state potential. Ocean Eng 208, 107445. https://doi.org/10.1016/j.oceaneng.2020.107445.

Kheirabadi, A.C., Nagamune, R., 2021a. Real-time relocation of floating offshore wind turbines for power maximization using distributed economic model predictive control. In: Proceedings of the 2021 American Control Conference (ACC). IEEE, New Orleans, LA, USA, pp. 3077–3081.

Kheirabadi, A.C., Nagamune, R., 2021b. A low-fidelity dynamic wind farm model for simulating time-varying wind conditions and floating platform motion. Ocean Eng 234, 109313. https://doi.org/10.1016/j.oceaneng.2021.109313.

Li, Y., Wu, Z., 2016. Stabilization of floating offshore wind turbines by artificial muscle based active mooring line force control. In: Proceedings of the 2016 American Control Conference (ACC). IEEE, Boston, MA, USA, pp. 2277–2282.

Li, S., Snaiki, R., Wu, T., 2021a. A knowledge-enhanced deep reinforcement learning-based shape optimizer for aerodynamic mitigation of wind-sensitive structures. Comput. Aided Civ. Infrastruct. Eng. 36, 733–746. https://doi.org/10.1111/mice.12655.

Li, S., Snaiki, R., Wu, T., 2021b. Active simulation of transient wind field in a multiple-fan wind tunnel via deep reinforcement learning. J. Eng. Mech. 147, 04021056. https://doi.org/10.1061/(ASCE)EM.1943-7889.0001967.

Lin, M., Porté-Agel, F., 2020. Power maximization and fatigue-load mitigation in a wind-turbine array by active yaw control: an LES study. J. Phys. Conf. Ser. 1618, 042036. https://doi.org/10.1088/1742-6596/1618/4/042036.

Nilsson, K., Ivanell, S., Hansen, K.S., Mikkelsen, R., Sørensen, J.N., Breton, S., Henningson, D., 2015. Large-eddy simulations of the lillgrund wind farm. Wind Energy 18, 449–467. https://doi.org/10.1002/we.1707.

Niu, Y., Lathi, P.P., Nagamune, R., 2023. Floating offshore wind farm control via turbine repositioning with aerodynamic force. In: Proceedings of the 2023 American Control Conference (ACC). IEEE, San Diego, CA, USA, pp. 2542–2547.

Porté-Agel, F., Wu, Y.-T., Chen, C.-H., 2013. A numerical study of the effects of wind direction on turbine wakes and power losses in a Large wind farm. Energies 6, 5297–5313. https://doi.org/10.3390/en6105297.

Powell, M.J.D., 1994. A direct search optimization method that models the objective and constraint functions by linear interpolation. In: Gomez, S., Hennart, J.-P. (Eds.), Advances in Optimization and Numerical Analysis, vol. 275. Springer Netherlands, Dordrecht, The Netherlands, pp. 51–67. ISBN 978-94-015-8330-5.

Raach, S., Schlipf, D., Sandner, F., Matha, D., Cheng, P.W., 2014. Nonlinear model predictive control of floating wind turbines with individual pitch control. In: Proceedings of the 2014 American Control Conference. IEEE, Portland, OR, USA, pp. 4434–4439.

Robertson, A., Jonkman, J., Masciola, M., Song, H., Goupee, A., Coulling, A., Luan, C., 2014. Definition of the Semisubmersible Floating System for Phase II of OC4. National Renewable Energy Laboratory, Golden, CO, USA, 1155123. NREL/TP-5000-60601.

Rodrigues, S.F., Teixeira Pinto, R., Soleimanzadeh, M., Bosman, P.A.N., Bauer, P., 2015. Wake losses optimization of offshore wind farms with moveable floating wind

turbines. Energy Convers. Manag. 89, 933–941. https://doi.org/10.1016/j.enconman.2014.11.005.
Shah, K.A., Meng, F., Li, Y., Nagamune, R., Zhou, Y., Ren, Z., Jiang, Z., 2021a. A synthesis of feasible control methods for floating offshore wind turbine system dynamics. Renew. Sustain. Energy Rev. 151, 111525. https://doi.org/10.1016/j.rser.2021.111525.
Shah, K.A., Li, Y., Nagamune, R., Zhou, Y., Ur Rehman, W., 2021b. Platform motion minimization using model predictive control of a floating offshore wind turbine. Theor. Appl. Mech. Lett. 11, 100295. https://doi.org/10.1016/j.taml.2021.100295.
Sierra-Garcia, J.E., Santos, M., Pandit, R., 2022. Wind turbine pitch reinforcement learning control improved by PID regulator and learning observer. Eng. Appl. Artif. Intell. 111, 104769. https://doi.org/10.1016/j.engappai.2022.104769.
Sørensen, A.J., 2011. A survey of dynamic positioning control systems. Annu. Rev. Control 35, 123–136. https://doi.org/10.1016/j.arcontrol.2011.03.008.
Steinbuch, M., de Boer, W.W., Bosgra, O.H., Peters, S.A.W.M., Ploeg, J., 1988. Optimal control of wind power plants. J. Wind Eng. Ind. Aerod. 27, 237–246. https://doi.org/10.1016/0167-6105(88)90039-6.
Swart, R., Coppens, C., Gordjin, H., Piek, M., Ruyssenaars, P., Schrander, J.J., Papalexandrou, M., Horalek, J., 2009. *Europe's Onshore And Offshore Wind Energy Potential : an Assessment Of Environmental And Economic Constraints*; EEA Technical Report. European Environment Agency, København, Denmark.
The MathWorks Inc, 2023. Simulink Design Optimization™.
Vermeer, L.J., Sørensen, J.N., Crespo, A., 2003. Wind turbine wake aerodynamics. Prog. Aero. Sci. 39, 467–510. https://doi.org/10.1016/S0376-0421(03)00078-2.
Wagenaar, J., Machielse, L., Schepers, J., 2012. Controlling Wind in ECN's Scaled Wind Farm. Energy research Centre of the Netherlands, Copenhagen, Denmark.
Xu, S., Murai, M., Wang, X., Takahashi, K., 2021. A novel conceptual design of a dynamically positioned floating wind turbine. Ocean Eng 221, 108528. https://doi.org/10.1016/j.oceaneng.2020.108528.
Zhang, J., Zhao, X., Wei, X., 2022. Reinforcement learning-based structural control of floating wind turbines. IEEE Trans. Syst. Man Cybern. Syst 52, 1603–1613. https://doi.org/10.1109/TSMC.2020.3032622.